Community-based Reconstruction and Simulation of a Full-scale Model of Region CA1 of Rat Hippocampus

Armando Romani[1,+], Alberto Antonietti[1], Davide Bella[1], Julian Budd[1,3], Elisabetta Giacalone[2], Kerem Kurban[1], Sára Sáray[3,4], Marwan Abdellah[1], Alexis Arnaudon[1], Elvis Boci[1], Cristina Colangelo[1], Jean-Denis Courcol[1], Thomas Delemontex[1], András Ecker[1], Joanne Falck[5], Cyrille Favreau[1], Michael Gevaert[1], Juan B. Hernando[1], Joni Herttuainen[1], Genrich Ivaska[1], Lida Kanari[1], Anna-Kristin Kaufmann[1], James Gonzalo King[1], Pramod Kumbhar[1], Sigrun Lange[5,6], Huanxiang Lu[1], Carmen Alina Lupascu[2], Rosanna Migliore[2], Fabien Petitjean[1], Judit Planas[1], Pranav Rai[1], Srikanth Ramaswamy[1], Michael W. Reimann[1], Juan Luis Riquelme[1], Nadir Román Guerrero[1], Ying Shi[1], Vishal Sood[1], Mohameth François Sy[1], Werner Van Geit[1], Liesbeth Vanherpe[1], Tamás F. Freund[3,4,*], Audrey Mercer[5,*], Eilif Muller[1,*], Felix Schürmann[1,*], Alex M. Thomson[5,*], Michele Migliore[2,*,+], Szabolcs Káli[3,4,*,+], and Henry Markram[1,*,+]

[1]Blue Brain Project, École polytechnique fédérale de Lausanne (EPFL), Campus Biotech, Geneva, Switzerland

[2]Institute of Biophysics, National Research Council (CNR), Palermo, Italy

[3]Institute of Experimental Medicine (KOKI), Eötvös Loránd Research Network, Budapest, Hungary

[4]Faculty of Information Technology and Bionics, Pázmány Péter Catholic University, Budapest, Hungary

[5]UCL School of Pharmacy, University College London (UCL), London, UK

[6]School of Life Sciences, University of Westminster, London, UK

*Co-senior authors

+Corresponding authors

May 17, 2023

Abstract

The CA1 region of the hippocampus is one of the most studied regions of the rodent brain, thought to play an important role in cognitive functions such as memory and spatial navigation. Despite a wealth of experimental data on its structure and function, it can be challenging to reconcile information obtained from diverse experimental approaches. To address this challenge, we present a community-driven, full-scale *in silico* model of the rat CA1 that integrates a broad range of experimental data, from synapse to network, including the reconstruction of its principal afferents, the Schaffer collaterals, and a model of the effects that acetylcholine has on the system. We have tested and validated each model component and the final network model, and made input data, assumptions, and strategies explicit and transparent. The flexibility of the model allows scientists to address a range of scientific questions. In this article, we describe the methods used to set up simulations that reproduce and extend *in vitro* and *in vivo* experiments. Among several applications in the article, we focus on theta rhythm, a prominent hippocampal oscillation associated with various behavioral correlates and use our computer model to reproduce and reconcile experimental findings. Finally, we make data, code and model available through the hippocampushub.eu portal, which also provides an extensive set of analyses of the model and a user-friendly interface to facilitate adoption and usage. This neuroscience community-driven model represents a valuable tool for integrating diverse experimental data and provides a foundation for further research into the complex workings of the hippocampal CA1 region.

Keywords

hippocampus, CA1, neuroscience community, large-scale compartmental modeling, data-driven.

1 Introduction

The hippocampus is thought to play a fundamental role in cognitive functions such as learning, memory, and spatial navigation (Morris et al., 1982; O'Keefe & Dostrovsky, 1971). It consists of three subfields of *cornu ammonis* (CA), CA1, CA2, and CA3 (see Amaral and Witter, 1989). CA1, for instance, one of the most studied, provides the major hippocampal output to the neocortex and many other brain regions (e.g. Soltesz and Losonczy, 2018). Therefore, understanding the function of CA1 represents a significant step towards explaining the role of hippocampus in cognition.

Each year the large neuroscientific community studying hippocampus contributes thousands of papers to an existing mass of empirical data collected over many decades of research (see Figure S1). Recent reviews have, however, highlighted gaps and inconsistencies in the existing literature (Bezaire & Soltesz, 2013; Pelkey et al., 2017; Sanchez-Aguilera et al., 2021; Wheeler et al., 2015). Currently, the community lacks a unifying, multiscale model of hippocampal structure and function with which to integrate new and existing data.

Computational models and simulations have emerged as crucial tools in neuroscience for consolidating diverse multiscale data into unified, consistent and quantitative frameworks that can be used to validate and predict dynamic behavior (Fan & Markram, 2019). However, constructing such models requires assigning values to model parameters, which often involves resolving conflicts in the data, identifying gaps in knowledge, and making explicit assumptions to compensate for any incomplete data. In order to validate the model, it must be tested under specific experimental conditions using independent sources of empirical evidence before the model can be used to generate experimentally testable predictions. Therefore, the curation of a vast range of experimental data is a fundamental step in constructing and parametrizing any data-driven model of hippocampus.

The challenge of incorporating these data into a comprehensive reference model of hippocampus, however, is considerable and calls for a community effort. While community-wide projects are common in other disciplines (e.g. Human Genome Project in bioinformatics, CERN in particle physics, NASA's Great Observatories program in astronomy - Aad and Abbott, 2015; Hood and Rowen, 2013; Rockström et al., 2009), they are a relatively recent development in neuroscience. OpenWorm, for example, is a successful, decade-long community project to create and simulate a realistic, data-driven reference model of the roundworm *Caenorhabditis elegans* (*C. elegans*) including its neural circuitry of ∼302 neurons to study the behavior of this relatively simple organism *in silico* (Gerkin et al., 2018; Szigeti et al., 2014). By contrast, for the hippocampus, with a circuit many orders of magnitude larger than *C. elegans*, models have typically been constructed with a minimal circuit structure on a relatively small scale and often their model parameters have been tuned with the goal of reproducing a single empirical phenomenon (see Sutton and Ascoli, 2021). Comparing the results from a variety of circuit models is problematic because they vary in their degree of realism and frequently rely on one or a few single neuron models making generalization of their findings difficult (see Sutton and Ascoli, 2021). While these focused models have led to valuable insights (see M. E. Hasselmo et al., 2020), this piecemeal approach fails to demonstrate whether these separate phenomena can be reproduced in a full circuit model without the need to adjust parameters.

Large-scale circuit models of hippocampus using realistic multi-compartment spiking neuronal models pioneered by Traub and colleagues (Traub et al., 1988, 1992, 2000; Traub & Miles, 1991) have been used to explain key characteristics of oscillatory activity observed in hippocampal slices and to examine the origins of epilepsy in region CA3. More recently, with significant increases in high-performance computing resources, Cutsuridis et al. (2010) in a microcircuit model of CA1 and notably Bezaire et al. (2016) in a full-scale CA1 model, have examined the contribution of diverse types of interneurons to the generation of prominent theta (4-12 Hz) oscillations. While these large-scale circuit models provide a more holistic approach, they still need to incorporate other features to improve their realism. For instance, to better reflect the highly curved shape of the hippocampus, an atlas-based structure that more closely mimics anatomy is required. Additionally, models need to employ pathway-specific short-term synaptic plasticity known to regulate circuit dynamics and neural coding (Tsodyks & Markram, 1997). While Yu et al. (2020) have constructed a down-scaled, atlas-based model of the rat dentate gyrus (DG) to CA3 pathway, there has to date been no atlas-based, full-scale model of rat CA1 (For a more detailed comparison of these models, see Table S2).

To initiate a community effort of this magnitude requires an approach that standardizes data curation and integration of diverse datasets from different labs and uses these curated data to construct and simulate a scalable and reproducible circuit automatically. A reconstruction and simulation methodology was introduced and applied at the microcircuit scale, for the neocortex (Markram et al., 2015) and the thalamus (Iavarone et al., 2023) and at full-scale for a whole neocortical area (Reimann et al., 2022). However, these models relied primarily on datasets collected specifically for the purpose rather than data sought from and curated with the help of the scientific community.

In this paper, we describe a community-driven reconstruction and simulation of a full-scale, atlas-based multiscale structural and functional model of the area CA1 of the hippocampus that extends and improves upon the approach described in Markram et al. (2015). To stimulate the model beyond its intrinsic circuitry, we have also modeled the synaptic input from the largest afferent pathway to CA1, the Schaffer collaterals (SC) axons from CA3, the input most commonly stimulated electrically in the experiments, and the neuromodulatory influence of cholinergic inputs, perhaps the most studied neuromodulator in the hippocampus (Teles-Grilo Ruivo & Mellor, 2013). We constrained all model parameters and data using available experimental data from different labs or explicit assumptions made when data were lacking. We extensively tested and validated each model component and the final network to assess its quality. To maximize realism of the simulations, we set up simulation experiments to represent as closely as possible the experimental conditions of each empirical validation. We demonstrated the broad applicability of the model by studying the generation of neuronal oscillations, with a specific focus on theta rhythm, in response to a variety of different stimulus conditions. Over time and with the help of the community, limitations of the model revealed by these processes can be addressed to improve upon it. To facilitate a widespread adoption by the community, we have developed a web-based resource to share the model and its components, open sourcing extensive analyses, validations, and predictions that can be accessed as a complement to direct interaction with the model (hippocampushub.eu). Finally, we have developed a massive online open course (MOOC) to introduce users to the building, analysis, and simulation of a rat CA1 microcircuit (https://www.edx.org/course/simulating-a-hippocampus-microcircuit) providing a smaller version of the full-scale model for education purposes.

2 Results

We divide the results section into model reconstruction, and model simulation and applications. These subsections represent two distinct processes: the reconstruction of the general model and its use to investigate specific scientific questions (see Table S1, for a list of abbreviations and acronyms used in the paper).

2.1 Model reconstruction

In this section, we describe how we reconstructed the main components of the model: the cornus ammonis 1 (CA1), its main afferents, the Schaffer collaterals (SC), and the effect of acetylcholine (ACh). We describe each model component as a compound model of several building blocks (Figure 1). For each building block, we show how we evolved from the sparse data available in the literature to the dense data necessary for the reconstruction process. We provide the source of the data, our assumptions and our rationale. Finally, we show validations of the building blocks to assess their robustness and validity. We describe the technical details briefly in Methods, and fully in Supplementary Methods.
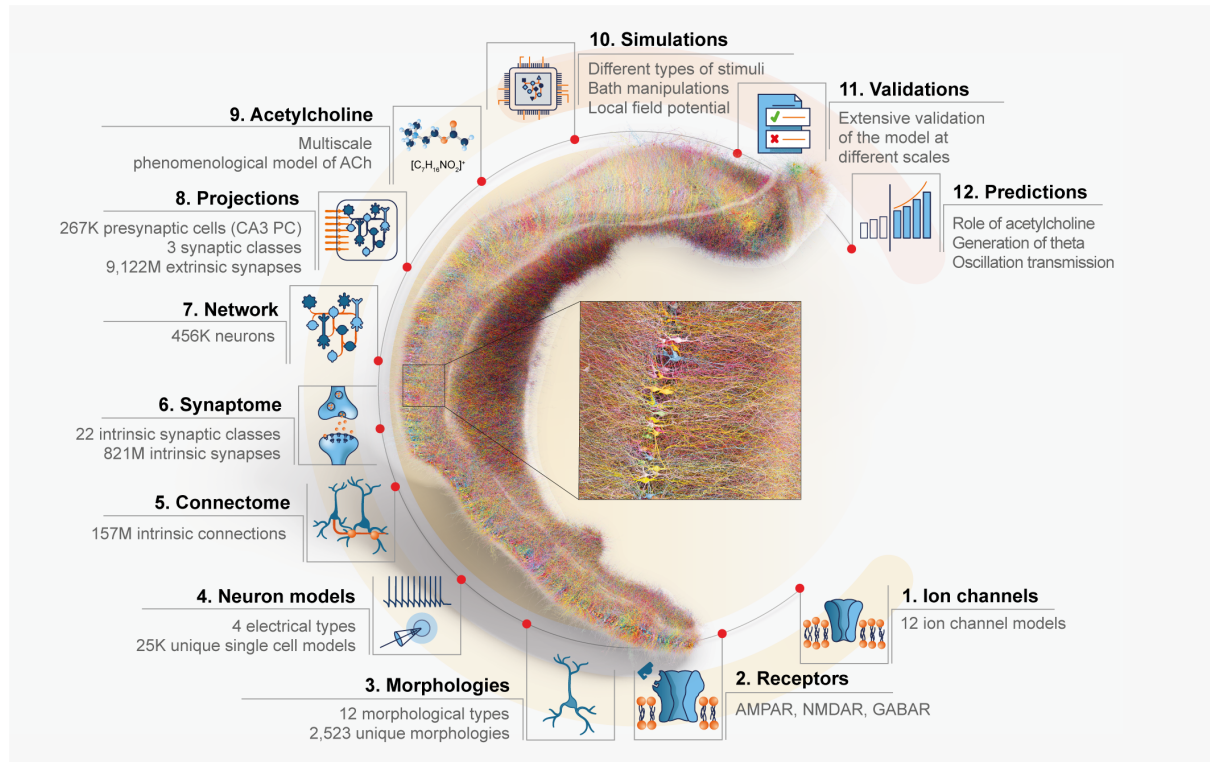
Figure 1: **Overview of the model and the reconstruction process.** A visualization of a full-scale, right-hemisphere reconstruction of rat CA1 region and its components. The number of cells is reduced to 1% for clarity, where neurons are randomly colored. The CA1 network model integrates entities of different spatial and temporal scales. The different scales also reflect our bottom-up approach to reconstruct the model. Ion channels (step 1) were inserted into the different morphological types (step 3) to reproduce electrophysiological characteristics and obtain neuron models (step 4). Neurons were then connected by synapses to generate an intrinsic CA1 connectome (step 5). For each intrinsic pathway, synaptic receptors (step 2) and transmission dynamics were assigned based on single neuron paired recording data (step 6) to create a functional intrinsic CA1 network model (step 7). The intrinsic CA1 circuit received synaptic input from CA3 via Schaffer collateral (SC) axons (step 8). The neuromodulatory influence of cholinergic release on the response of CA1 neurons and synapses was modeled phenomenologically (step 9). The dynamic response of the CA1 network was simulated with a variety of manipulations to model *in vitro* and *in vivo*, intrinsic and extrinsic stimulus protocols while recording intracellularly and extracellularly (step 10) to validate the circuit at different spatial scales against specific experimental studies (step 11) and to make experimentally testable predictions (step 12).

2.1.1 Cornu ammonis 1 (CA1)

We reconstructed a full-scale model of the CA1 field of the rat hippocampus (Figure 1) by following and adapting the method described in Markram et al. (2015). For the neuron models, we defined morphological type (m-type) and electrical properties type (e-type) of rat CA1 based on experimental datasets. For m-types, we used two datasets (from young adult Sprague Dawley and Wistar rats) which include 43 morphological reconstructions of neurons belonging to 12 m-types (Table S3, https://www.hippocampushub.eu/model/experimental-data/neuronal-morphology/). In particular, we considered one type of excitatory neuron, the pyramidal cell (PC), and 11 types of inhibitory neurons:

axo-axonic cell (AA), two types of bistratified cell (BS), back-projecting cell (BP), cholecystokinin (CCK) positive basket cell (CCKBC), ivy cell (Ivy), oriens lacunosum-moleculare cell (OLM), perforant pathway associated cell (PPA), parvalbumin positive basket cell (PVBC), Schaffer collateral associated cell (SCA), and trilaminar cell (Tri). We subsequently repaired, scaled and cloned the neurons to produce a morphology library of 2,592 cells (https://www.hippocampushub.eu/model/digital-reconstructions/neurons/).

To validate the resulting morphology library, we considered the distributions of 21 different morphological features and computed a similarity score between original and cloned morphologies. We report the average scores grouped per feature and per m-type in Figure S2 and show that the similarity scores of the clone morphologies are in agreement with the original samples (see supplementary methods) . We also conducted correlation tests for different neurites between original and cloned morphologies (apical dendrites: $R = 0.99$, $p = 1.57 \times 10^{-42}$, basal dendrites: $R = 0.99$, $p = 1.56 \times 10^{-27}$, axons: $R = 0.99$, $p = 1.03 \times 10^{-26}$). In addition, we compare the topological features of the original, repaired, and cloned morphologies using Topological Morphology Descriptor (TMD), as described in Kanari et al. (2018). In Figure S3, we present the persistence diagrams of the three stages, which indicate an increase in morphological diversity introduced by the cloning process. The details of the topological differences per m-type are presented in Figures S4 and S5.

For e-types, we used one dataset (from Sprague Dawley rats), which includes 1,456 experimentally obtained somatic voltage traces from 154 single cell recordings. We classified the recordings into four different e-types: classical accommodating for pyramidal cells and interneurons (cACpyr, cAC), bursting accommodating (bAC), and classical non-accommodating (cNAC), according to the well-established classification of Petilla Nomenclature (Petilla Interneuron Nomenclature Group et al., 2008) (https://www.hippocampushub.eu/model/experimental-data/neuronal-electrophysiology/). By analyzing our datasets, and where necessary, including data from the literature, each m-type can have one or multiple e-types with different probability. We used this information to derive the morpho-electrical type (me-type) composition (Table S4, https://www.hippocampushub.eu/model/reconstruction-data/cell-composition/).

We combined electrophysiological features (e-features) extracted from the single cell recordings with 34 morphologies to produce 39 single cell models (or electrical models, e-models) (Ecker et al., 2020; R. Migliore et al., 2018) (https://www.hippocampushub.eu/model/reconstruction-data/neuron-models/). From this initial pool, we excluded three models because they did not correspond to any me-types described experimentally. We combined the remaining 36 e-models with 2,973 morphologies to obtain a library of 26,112 models that matched the initial set of e-features (https://www.hippocampushub.eu/model/reconstruction-data/neuron-models/). In the case of pyramidal cells, we further validated the e-models in terms of back-propagating action potential (BPAP) showing a close correlation to experimental findings (Golding et al., 2001) ($R = 0.878$, $p = 0.121$) and post-synaptic potential (PSP) attenuation (Magee & Cook, 2000) ($R = 0.846$, $p = 0.001$) (Figure S6).

To move from single cell to network level, we started to define the volume of the region (Figure S7). We took a publicly available atlas reconstruction of the hippocampus (http://cng.gmu.edu/hippocampus3d/) (Ropireddy et al., 2012) and considered only the CA1 region. Despite the fact that CA1 layers (stratum oriens (SO), stratum pyramidale (SP), SO. stratum radiatum (SR), and

182 stratum lacunosum moleculare (SLM)) were annotated in the original atlas, the presence of artifacts
183 (see S1.13.1) made using the volume challenging with our existing algorithms. To alleviate the prob-
184 lem, we followed additional curation steps. First, we algorithmically divided the volume into layers
185 with a fixed ratio of their thicknesses (SO: 0.258 SP: 0.090 SR: 0.428 SLM: 0.224), according to
186 the values extracted from the Sprague Dawley and Wistar dataset (https://www.hippocampushub.
187 eu/model/experimental-data/layer-anatomy/). Then we defined vector fields and a coordinate sys-
188 tem that follow the three axes of the hippocampus (longitudinal, transverse, and radial) (Figure 2,
189 https://www.hippocampushub.eu/model/experimental-data/layer-anatomy/). These extra features in-
190 formed the subsequent processes of cell placement and circuit analysis.
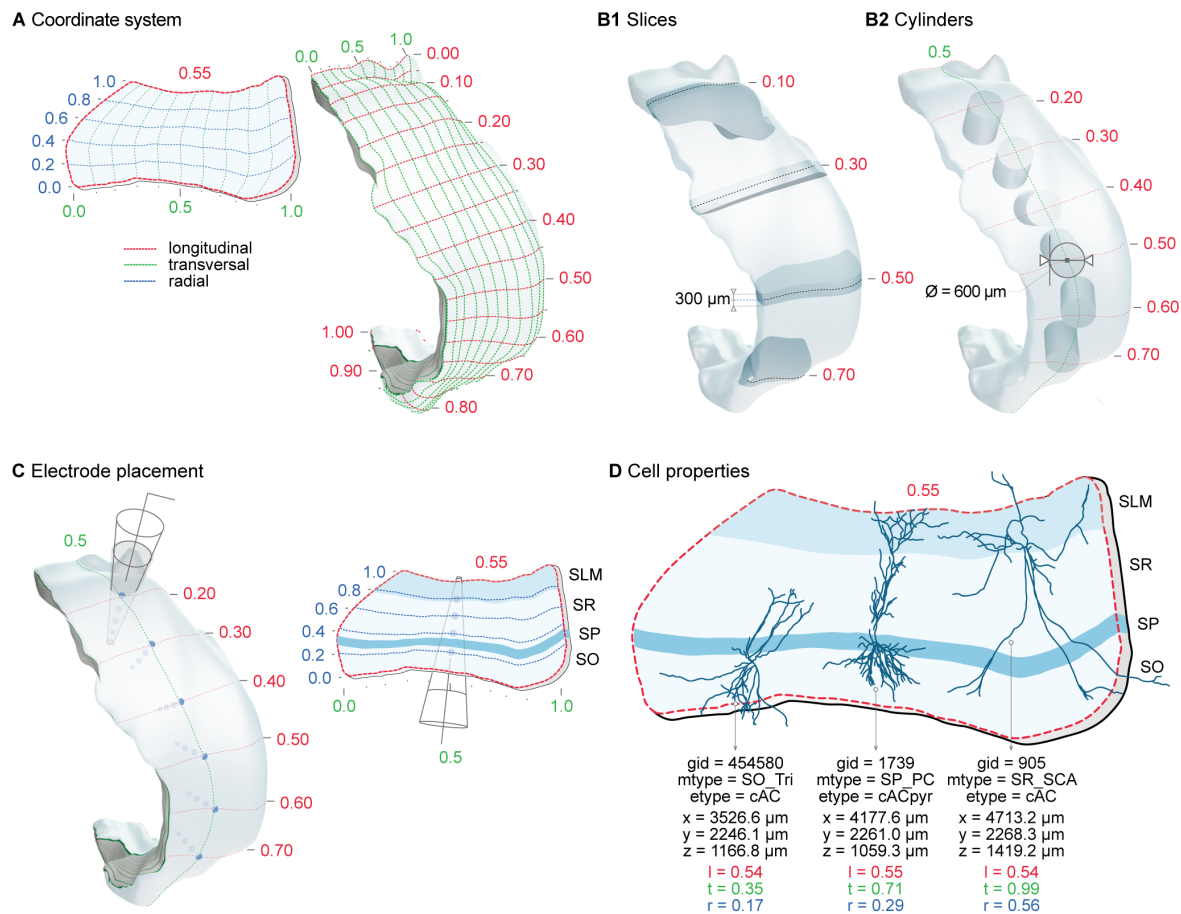
8

Figure 2: **Custom CA1 parametric coordinates system used as spatial reference for circuit building, circuit segmentation, and for simulation experiments**. A. Longitudinal (l, red), transverse (t, blue) and radial (r, green) axes of the CA1 volume are defined parametrically in range [0,1]. Left: Slice from volume shows radial depth from SO/alveus (r=0) to SLM/pial (r=1) and transverse extent from CA3/proximal CA1 (t=1) to distal CA1/subiculum (t=0) boundaries. Right: Full volume shows surface grid of transverse vs longitudinal axes. B. Circuit segmentation for analysis and simulation. (B1) Coordinates system used to select CA1 slices of a given thickness at specific locations along longitudinal axis. (B2) Coordinate system used to select cylinder of a given surface diameter throughout entire depth of CA1 at specific positions along longitudinal axis. C. Extracellular electrode placed at a given surface position (right) and channels at selected laminar depth (left) in CA1 volume. D. Each neuron in the circuit defined by a unique general identifier (gid), its morphological type (m-type), electrical type (e-type), spatial xyz-coordinates and parameterized ltr-coordinates.

Once we had defined the volume, we populated it with the single cell models according to our constraints on cell composition (Figure S8A-B, Table S3). Despite the multiple constraints of the cell placement, we could include 2,523 neuron morphologies out of the 2,592 in the morphology 25,355 neuron models out of the 26,112 in the neuron model library into the volume. Subsequently, we validated the cell composition ($R = 0.999$, $p = 1.31 \times 10^{-28}$) and pyramidal cell density to guarantee a consistency with input data (Figure S9B-C, Table S3). We also validated cell densities using an additional dataset

9

197 (Figure S9C, Table S5). The discrepancies can be explained by the absence of some cell types and by
198 our strategy to compensate for this lack by increasing the number of cells in other layers. In fact, since
199 most of our reconstructions were experimentally sampled from the SP, the density in SP is higher than
200 the value reported in literature while it is lower in other layers. Despite these discrepancies, we have a
201 good match with experimental data ($R = 0.999$, $p < 0.0001$) (Figure S9C).

202 We positioned the cells following a series of rules that describe how different neurite types target the
203 different layers (Figure S8C-D, Table S6), and we validated the resulting cell placements visually (Figure
204 S9A). In general, cells in our model follow the curvature of the hippocampus and the different parts of
205 the cells target the expected layers. However, a closer look may reveal several artifacts. First, some
206 branches can be present outside the volume. In some cases, there is clear experimental evidence that
207 neurites extend beyond CA1. For example, the PC axons and OLM dendrites invade the alveus, back-
208 projecting neurons project to CA2, CA3 and DG. In other cases, there is no clear evidence that the
209 biological morphologies comply with the layer boundaries. Another artifact is that neurites may not
210 follow the exact curvature of the layers. Experimentally, cells were sampled from some specific areas
211 but in the model, they may be positioned in locations with different curvatures. We could overcome
212 these two limitations with morphology synthesis (Kanari et al., 2022), but this approach is beyond the
213 scope of this paper.

214 To connect the placed neurons, we used the connectome algorithm previously described in Reimann
215 et al. (2015) and initially applied in the cortical model of Markram et al. (2015). This algorithm
216 has been demonstrated to recreate higher-order topological features (Gal et al., 2017). In brief, the
217 algorithm searches for co-localization of axon and postsynaptic neurons. To identify a potential synapse
218 (touch or apposition), segments have to be within a certain distance (maximum touch distance). After
219 identifying all potential synapses, a subsequent step (pruning) discards those that exceed the known
220 bouton densities (Table S7) and number of synapses per single axon connection (Table S9). While this
221 algorithm was originally developed for cortical connections, we found that it generalized effectively to
222 the hippocampus with an important modification.

223 Based on the maximum touch distances used in the cortex model of $2.5\,\mu m$ and $0.5\,\mu m$ for pyramidal cells
224 (PCs) and interneurons (INTs), respectively, interpreted as the presence or absence of dendritic spines,
225 our CA1 model showed that PCs predominantly made their synapses with other PCs (97.4%) rather than
226 with INTs (2.6%). This finding is significantly different from experimental evidence in the CA1 (PC:
227 39.2%, INT: 53.8%, unknown: 6.9%, scaled up after distributing the unknown cells proportionally to
228 reach a ratio of PC: 42.2%, INT: 57.8%) (Takács et al., 2012). We reasoned that this large discrepancy
229 with experimental data could not be explained solely by the absence of certain cell types in our model.
230 Instead, we hypothesized that there might be another biological mechanism that makes the connections
231 among PCs less probable and the connections between PCs and INTs more probable than chance. Since
232 we did not have a complete understanding of the underlying mechanism, we decided to optimize the
233 maximum touch distance and found that a value of $1.0\,\mu m$ and $6.0\,\mu m$ for the distances to PCs and
234 INTs, respectively, represented the minimum values that allowed us to match experimental data and
235 give some flexibility in the subsequent synapse pruning (see Supplementary methods for details).

236 Once the connectome had been constrained, it consisted of about 821 million synapses. We validated

10

237 and analyzed it extensively to make predictions about uncharacterized pathways (Figures S11, S12, S13,
238 and S14). First, we validated the bouton density and number of synapses per connection to confirm
239 that we could still match the data we used to constrain the connectome (bouton density: $R = 0.909$,
240 $p = 0.0120$; number of synapses per connection: $R = 0.992$, $p = 2.41 \times 10^{-9}$, Figure S11 and Tables S7
241 and S9). We observed that distributions of connection probability (Figure S12A), convergence (Figure
242 S13A) and divergence (Figure S14A) had the same skewed shape obtained experimentally (Giacopelli
243 et al., 2021). In the case of connection probability, experimental data did not allow comparison (Figure
244 S12C, Table S8). Typically, only the slice thickness and the maximum distances between neuron pairs
245 tested was given. For convergence, we compared our results with Megias et al. (2001) to validate the
246 synapses on different compartments of pyramidal cells and our model appears to be in a good agreement
247 with reported values ($R = 0.988$, $p = 0.012$, Figure S13C). For divergence, we had more datasets. First,
248 for several m-types, we had the total number of synapses they form (Table S10). However, the model did
249 not match the experimental data well ($R = 0.524$, $p = 0.2864$, Figure S14C). Many factors may have
250 contributed to this difference: e.g., the small sample size in many experiments (but also in the model
251 since we started from the few example reconstructions), or high variability in axon lengths preserved in
252 the experimental slices. We compared divergence also in terms of the percentage of synapses formed
253 with PCs or INTs (Figure S14D, Table S11) and validated distribution of diverging synapses in the
254 different layers (SO: $R = 0.798$, $p = 0.057$; SP: $R = 0.905$, $p = 0.013$; SR: $R = 0.813$, $p = 0.049$;
255 SLM: $R = 0.999$, $p = 4.11 \times 10^{-8}$, Figure S14E, Table S12).

256 Starting from anatomical connections, we defined synaptic parameters following the methodology de-
257 scribed in Ecker et al. (2020), which involved integrating the available datasets into a model of synaptic
258 transmission encompassing stochastic neurotransmitter release and short-term plasticity (STP) (Figure
259 S15). Since we did not make changes to the synapse model architecture, we used most of the parameters
260 identified by Ecker and colleagues. In Tables S13 and S14, we report the values of the pathway-specific
261 model parameters for the 22 classes of pathways we have identified. In addition, we performed two
262 validations to determine how close to experimental data the model is in terms of post-synaptic poten-
263 tial (PSP) amplitudes (Figure S15D, R = 0.999, $p = 1.65 \times 10^{-19}$) and post-synaptic current (PSC)
264 coefficient of variation (CV) of the first peak (Figure S15E, $R = 0.840$, $p = 0.018$) for the pathways
265 with available electrophysiological recordings.

266 After having constrained and validated the synapses, the CA1 network was essentially fully constructed.
267 However, an isolated CA1 does not have substantial background activity, and normally the network is
268 driven by external inputs. In the following section, we describe the reconstruction of Schaffer collaterals,
269 a major input to CA1. This input provides the largest proportion of excitatory synapses to CA1 and
270 accounts for 92% of synapses in the model.

2.1.2 Reconstruction of Schaffer collaterals (SC)

272 CA1 is not known to contain pacemaker cells and the only spontaneous activity is due to the spontaneous
273 synaptic release (Le Bon-Jego & Yuste, 2007). While we can still use the model to reproduce experiments
274 where currents are artificially injected, the capability of the model was augmented with the reconstruction
275 of Schaffer collaterals, the most studied pathway in the hippocampus (Dumas et al., 2018; Szirmai et al.,
276 2012).

277 First, to reconstruct the anatomy of Schaffer collaterals, we constrained the number of CA3 PCs ap-
278 plying the ratios between CA3 PCs and CA1 PCs, as reported by Bezaire and Soltesz (2013), resulting
279 in 267,238 presynaptic neurons. We modeled each CA3 pyramidal cell to have the same probability
280 of contacting CA1 cells regardless of their longitudinal positions (Table S15) since we had scarce to-
281 pographical data. We distributed synapses uniformly along the transverse and longitudinal axes, while
282 along the radial axis, we followed a layer-wise distribution as reported by Bezaire and Soltesz (2013)
283 (Figure 3A-C). In addition, we constrained the convergence of SC synapses on PCs and interneurons
284 to mean values of 20,878 and 12,714, respectively (Bezaire & Soltesz, 2013). The resulting Schaffer
285 collateral input added 9,122 billion synapses to CA1, 11.1 times more numerous than intrinsic synapses.
286 As expected, mean synapse convergence on PCs and interneurons matches experimental values used as
287 constraints (one-sample t-test, $p = 0.957$ for PCs and $p = 0.990$ for INTs). Interestingly, the variability
288 in the model is comparable with the upper and lower limits identified experimentally by Bezaire and
289 Soltesz (2013) (model PC: 20,878 $\pm$ 5,867 synapses and experimental PC: 13,059 - 28,697, model
290 INT: 12,714 $\pm$ 5,541 and experimental INT 7,952 - 17,476, Figure 3D-E). Most of the connections
291 between each CA3 PC and each CA1 neuron have a single synapse (1.0 $\pm$ 0.2 synapses/connection,
292 Figure S16A), coherent with what has been previously reported (Bezaire & Soltesz, 2013). Finally, the
293 resulting divergence from a single CA3 PC is 34,135 $\pm$ 185 synapses (Figure S16A), close to the higher
294 end of the ranges measured by Li et al. (1994), Sik et al. (1993), and Wittner et al. (2007) (15,295 -
295 27,440, Figure S16B).

296 We found limited data on synaptic parameters for the CA3-CA1 pathway in the literature, particularly in
297 relation to CA1 interneuron recordings, making parameterizing the synaptic input especially challenging
298 (Tables S16 and S17). This can be partly explained because the CA3 afferent pathway is sparsely
299 connected to CA1, so the chance of obtaining paired CA3-CA1 neuronal recordings is small between
300 PC-PC and much smaller from PC to interneurons (Debanne et al., 1995; Milstein et al., 2015; Sayer
301 et al., 1990; Wierenga & Wadman, 2003). Accordingly, rather than applying the usual procedure for
302 synaptic parametrization (Ecker et al., 2020), instead we considered SC→PC and SC→INT projections
303 separately. In both cases, we set the short-term plasticity (STP) parameters according to Wierenga and
304 Wadman (2003). Then, we ran a two-step procedure where we used the available data to optimize the
305 missing parameters (Figure S16C). Finally, we validated SC projections using Sasaki et al. (2006), where
306 the authors examined the basic input-output (I-O) characteristics of SC projections *in vitro*.

307 For SC→PC synapses, the first step optimized the peak synaptic conductance (0.85 ± 0.05 nS) and the
308 size of the readily releasable pool N$_{RRP}$ (12 vesicles) by matching the distribution of EPSP amplitudes
309 as measured by Sayer et al. (1990) (Figure 3F, experiment: 0.14 ± 0.11 mV, CV = 0.76, model:
310 0.15 ± 0.12 mV, CV = 0.80). We also performed a z-test to compare experimental and model EPSP
311 amplitudes ($p = value$: 0.709). The second step optimized the values of rise and decay time constants
312 of AMPA receptors (respectively 0.4 ms and 12.0 $\pm$ 0.5 ms) by matching the EPSP dynamics as
313 reported experimentally by Sayer et al. (1990) (Figure S16C, 10-90% rise time model: 5.4 ± 0.9 ms and
314 experiment: 3.9 ± 1.8 ms, half-width model: 20.3 ± 2.9 ms and experiment: 19.5 ± 8.0 ms, decay time
315 constant model: 19.5 ± 2.5 ms and experiment: 22.6 ± 11.0 ms).

316 In the case of SC→INT synapses, we followed the distinction identified by Glickfeld and Scanziani (2006)

12

317 and divided the interneurons into cannabinoid receptor type 1 negative (CB1R-) and positive (CB1R+).
318 First, we optimized the peak conductance (CB1R-: 15.0 $\pm$ 1.0 nS, CB1R+: 1.5 $\pm$ 0.1) and the N_{RRP}
319 (CB1R-: 2, CB1R+: 8) to obtain the $EPSC_{INT}/EPSC_{PC}$ ratios similar to experimental measurements
320 (Glickfeld & Scanziani, 2006) ($EPSC_{CB1R-}/EPSC_{PC}$ model 6.950 ± 9.200 and experiment $8.15 \pm$
321 6.00, $EPSC_{CB1R+}/EPSC_{PC}$ model 1.27 ± 1.78 and experiment 1.09 ± 1.44, Figure 3G-H). We also
322 made the comparison between model and experimental data using z-test (CB1R+: $p - value = 0.18$,
323 CB1R-: $p - value = 0.06$). Then, we optimized the rise and decay constants of AMPA receptors
324 (respectively 0.1 ms and 1.0 $\pm$ 0.1 ms for all interneurons) to match the correct timing in the EPSP-
325 IPSP sequence (Pouille & Scanziani, 2001) (model: 2.69 ± 1.18 ms, experiment: 1.9 ± 0.6, Figure
326 S16D). This short latency between the EPSP (triggered by the SC→PC stimulation) and the IPSP
327 (triggered by the di-synaptic loop SC→INT→PC) makes effective feedforward inhibition possible, a key
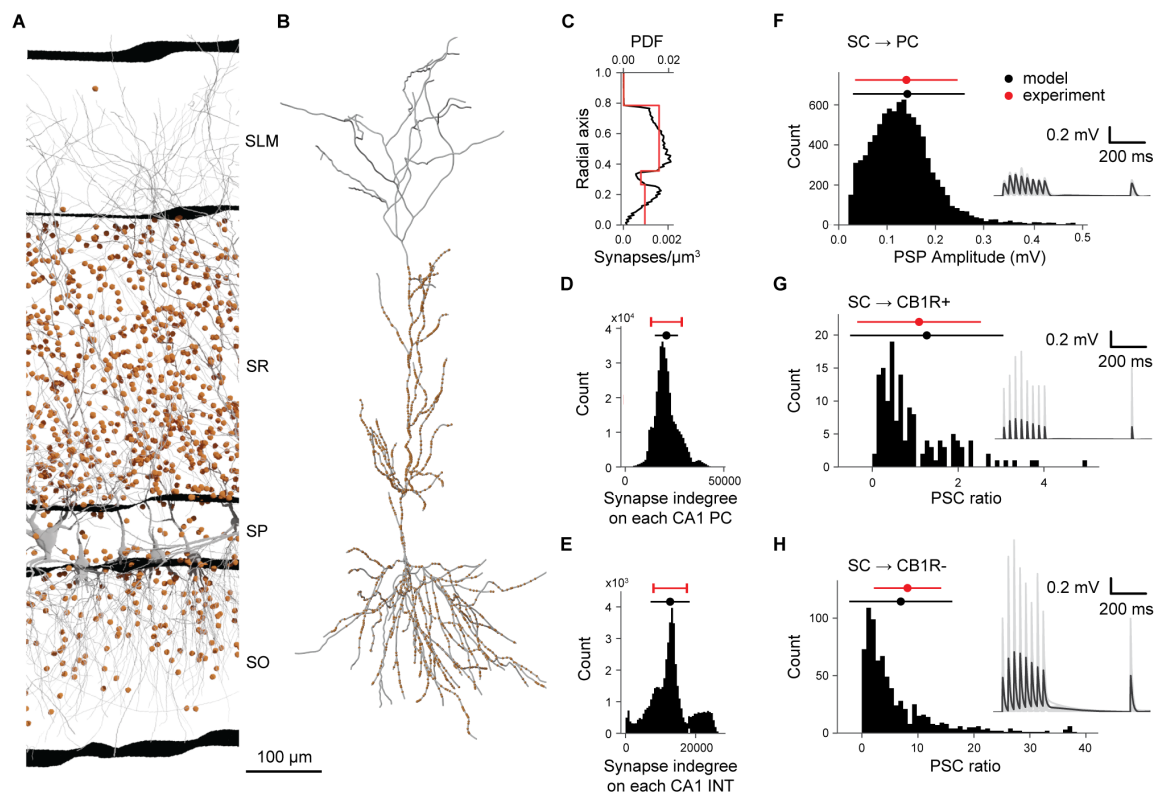328 aspect for the transmission of oscillations from CA3 to CA1.

Figure 3: **Schaffer collaterals anatomy and physiology**. A. Section of a slice of the dorsal CA1 showing 5 neurons in gray and SC synapses in orange (10% of the existing ones). B. Example of SC synapse placement (orange dots) on one reconstructed PC (in grey). C. Density of SC synapses (lower x axis, reported in synapses/μm^3) and probability density function (upper x axis) at different depths (radial axis percentage, from 0 to 1). The black line reports the measured densities in the reconstructed circuit, while the red line indicates the values measured experimentally (one value per layer). D-E. Distributions of afferent synapses from SC to pyramidal cells (D) and interneurons (E) (20,878 $\pm$ 5,867 and 12,714 $\pm$ 5,541 synapses, respectively). F. Fitting results of SC $\rightarrow$ PC synapses. The plot reports the distribution of PSP amplitudes computed over the 10,000 pairs of pre and postsynaptic neurons. On top, experimental (in red) and model (in black) mean and standard deviation values are reported with a dot and a bar, respectively. G-H. Fitting results of SC $\rightarrow$ CB1R+ (G) and SC $\rightarrow$ CB1R- interneurons synapses. CB1R+ interneurons are PPA, CCKBC, and SCA, while other interneurons are CB1R-. The plots report the distribution of the PSC ratio computed over the 1000 pairs of SC $\rightarrow$ INT, grouped by interneuron class (i.e., CB1R+ or CB1R-). Insets in panels F-H report voltage membrane traces of 10 randomly selected pairs of SC$\rightarrow$ PC, SC $\rightarrow$ CB1R+, and SC $\rightarrow$ CB1R- interneurons, respectively. The presynaptic SC is stimulated to fire 8 times at 30 Hz, plus a recovery pulse after 500 ms from the last spike of the train. Solid black lines represent mean values, and shaded gray areas the standard deviation. Scale bars: 0.2 mV and 200 ms.

To validate the SC projections, we compared the model results with the I-O characteristics reported in Sasaki et al. (2006). I-O of SC-CA1 is thought to be dominated by feedforward inhibition, which increases the dynamic range of the network and linearizes the I-O curve (Pouille et al., 2009; Sasaki et al., 2006). Application of a gamma-aminobutyric acid receptor (GABA$_A$R) antagonist such as gabazine

blocks the feedforward inhibition and drastically reduces the dynamic range of the network resulting in an I-O curve that saturates very quickly. We set up the simulations to be as close as possible to the experimental conditions (slice of $300\,\mu\mathrm{m}$, Ca^{2+} $2.4\,\mathrm{m\,M}$, Mg^{2+} $2.4\,\mathrm{m\,M}$, $32\,°\mathrm{C}$) (Figure 4A). To match the metholodology of Sasaki et al. (2006), we randomly sampled 101 neurons in the slice to find how many SC axons were required to make all 101 fire. As in the experiment, this represented respectively 100% of the output and 100% of input. From this point, we tested a decreasing number of SC fibers and recorded how many neurons fire. To assess the role of feedforward inhibition, we repeated the simulation by cutting the connections from interneurons, mimicking the effect of gabazine. The model I-O curves in both control and "no GABA" conditions approximated the experimental measurements well (Figure 4B). The model captured the quasi-linearization of the I-O response in control conditions (Pearson R = 0.992, p-value = 2.56×10^{-9}). Looking at the behavior following the stimulation at 50% of this intensity (Figure 4C) in control conditions, the spiking activity of CA1 SP neurons is rather weak and rapidly suppressed by the feedforward inhibition. However, without GABAergic inhibition, CA1 SP neurons fire at high frequency (up to 200 Hz) and for more than 50 ms.
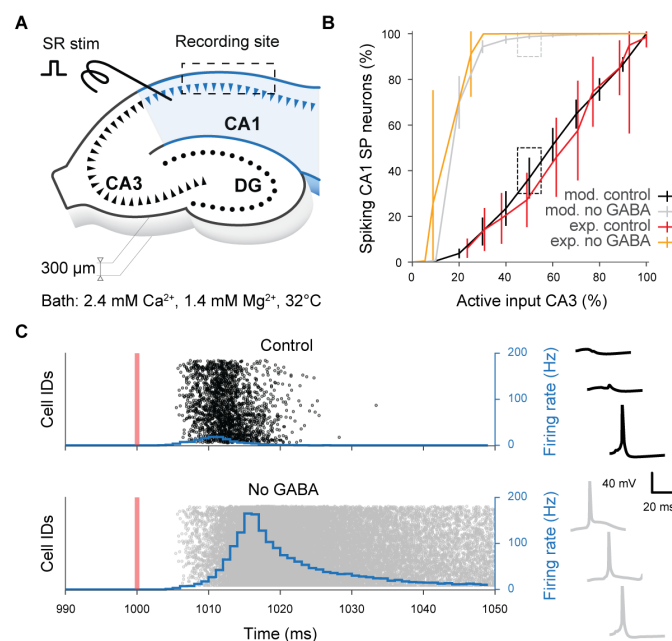

Figure 4: **Schaffer collaterals validation**. Effect of the feedforward inhibition on the input-output relationship of the network illustrated in a slice experiment. A. The illustration (redrawn from Figure 1A, (Sasaki et al., 2006)) shows the *in silico* experimental setup tailored to the experiment presented in Sasaki et al. (2006). B. Without GABA (orange line for experimental data, gray for model results), most of the SP neurons are recruited as soon as the number of SCs increases. With GABA (red line for experiments, black for model), the feedforward inhibition linearizes the response allowing a more modular activation of the cells in response to an increasing input. The dashed boxes identify the condition (50% of active SC) that is used to show the model's results in panel C. C. Raster plots of SP neurons in response to the SC stimulation (orange vertical line) with the overlaying firing rate (blue). On the right, membrane voltage traces of three randomly selected SP neurons in control (black) and no GABA (gray) conditions. Scale bars: 40 mV and 20 ms.

347 While the Schaffer collaterals do not represent the only input to CA1, they can account for the majority
348 of the excitatory synapses and represent a prototype for modeling other inputs. Finally, as demonstrated
349 in the Simulation and Applications section, the SC allows us to deliver realistic synaptic inputs to the
350 network and significantly increases the capabilities of the model. Indeed, network dynamics are not only
351 shaped by the trafficking of spikes among regions, but there is an important phenomenon that has a
352 profound impact on the network behavior: neuromodulation.

2.1.3 Cholinergic modulation

354 The behavior of the hippocampus is shaped by several neuromodulators, with acetylcholine (ACh)
355 among the most studied. Cholinergic fibers originate mainly from the medial septum and have been
356 correlated with phenomena such as theta rhythm, plasticity, memory retrieval and encoding, as well as
357 pathological conditions such as Alzheimer's disease (Dannenberg et al., 2017). This section describes
358 the reconstruction of a phenomenological model of ACh, quantifying the effects of ACh on cells and
359 synapses, and developing a novel method to integrate available experimental data (Tables S18 and
360 S19, Figure 5A-B). The data used to build the model was obtained from *in vitro* application of various
361 cholinergic agonists such as ACh and carbachol (CCh); here we assume that their effects are comparable
362 (Colangelo et al., 2019).

363 Our method allows the integration of disparate datasets, including the effects of ACh on resting mem-
364 brane potential and firing frequency. This is achievable because we can estimate the net current that is
365 required to evoke the corresponding changes in membrane potential or firing rate, for a given concen-
366 tration of ACh.

$$I_{depol} = \frac{0.567 ACh^{0.436}}{100^{0.436} + ACh^{0.436}} \tag{1}$$

367 where I_{depol} is the depolarizing current (in nA) and ACh is the neuromodulator concentration in µM (fit
368 $R^2 = 0.691$, $N = 28$, Figure 5AC).

369 We also include the effect of ACh on synaptic transmission, where ACh seems to act principally at the
370 level of release probability (M. E. Hasselmo, 2006; Tsodyks & Markram, 1997; D. Yang et al., 2021).

$$U_{SE} = \frac{1.0 ACh^{-0.576}}{4.541^{-0.576} + ACh^{-0.576}} \tag{2}$$

371 where U_{SE} is the release probability. (fit $R^2 = 0.667$, $N = 27$, Figure 5BD).

372 Once we had constrained the effect of ACh on neuron excitability and synaptic transmission, we validated
373 the effect of ACh at the network level. Available data (Table **??**) allowed a qualitative, although not
374 a precise validation of the model. In particular, we performed *in silico* bath application of ACh and
375 simulated a wide range of concentrations (from $0\,µM$ (i.e., control condition) to $1000\,µM$) (Figure 5E-
376 F). We observed a sub-threshold increase in the membrane potential of all neurons for values of ACh
377 lower than $50\,µM$, without any significant change in spiking activity. At intermediate doses (i.e., $100\,µM$

378 and 200 μM), the network shifted to a more sustained activity regime. Here, we observed a generalized
379 increase in firing rate as ACh concentration increased and a progressive build-up of coherent oscillations
380 whose frequencies ranged from 8 to 16 Hz (from high theta to low beta frequency bands). The correlation
381 peak between CA1 neurons occurred at 200 μM ACh (Figure 5G-H). At very high concentrations (i.e.,
382 500 μM and 1000 μM) we observed a decrease in the power of network oscillations, which was further
383 confirmed by analysis of local field potential (LFP) (Figure 5I). Power spectral density (PSD) analysis
384 showed a maximum absolute amplitude for 200 μM ACh with a peak frequency of ∼15 Hz (Figure
385 5J-K). Higher concentrations decreased the maximum amplitude of the PSD while the peak frequency
386 converged toward 17 Hz (Figure 5K).

387 Thus, we predict the emergence of three different regimes at low, intermediate, and high cholinergic
388 stimulation. The heterogeneity of the methodologies used to establish ACh influences on network
389 activity confounds the interpretation of the reports of the effects of ACh, and it is yet unclear whether
390 the network behavior we observe is validated by experimental findings. For instance, some research
391 shows that cholinergic agonism induces oscillations in isolated CA1 slices (Pietersen et al., 2014), but
392 several other studies show that while CCh evokes oscillations in CA3, and these can be transmitted to
393 CA1 via SC, it fails to induce oscillations in the CA1 region (Bianchi & Wong, 1994; Fellous & Sejnowski,
394 2000; Fisahn et al., 1998; J. H. Williams & Kauer, 1997). Arguably, there are no evident reasons to
395 justify the observed discrepancy, even though the possibility that CA1 mini slices were contaminated by
396 adjacent regions cannot be excluded. Moreover, even though *in vivo* ACh release and the emergence
397 of theta waves in the CA1 region are tightly correlated (Zhang et al., 2010), some authors report
398 that ACh's role is to increase the power and the coherence of the oscillations rather than generating
399 them (Vandecasteele et al., 2014). For a more exhaustive recapitulation of the different findings and
400 the methodologies applied, we redirect the reader to Table S20. In our CA1 model, progressive ACh
401 application induced a build-up of oscillatory activity, differently than in a previous model of neocortical
402 ACh release (Ramaswamy et al., 2018), where cholinergic stimulation caused desynchronization of
403 network activity at comparable concentrations. It's interesting to notice that even though the effects of
404 ACh release are roughly the same (generalized depolarization and decreased synaptic release probability)
405 the impact on network activity is drastically different in the two reconstructed microcircuits.

406 Capturing the relationship between cholinergic agonist application and subsequent local effects allows
407 a more rigorous description of the phenomenon and the prediction of the effect of virtually any ACh
408 concentration at synapse, neuron, and network level. The introduction of ACh allows the model to
409 reproduce a larger set of experiments in which ACh or its receptor agonists are necessary (see, for
410 example, Sections 2.2.1 and 2.2.2). Finally, the model of ACh can be used as a prototype to introduce
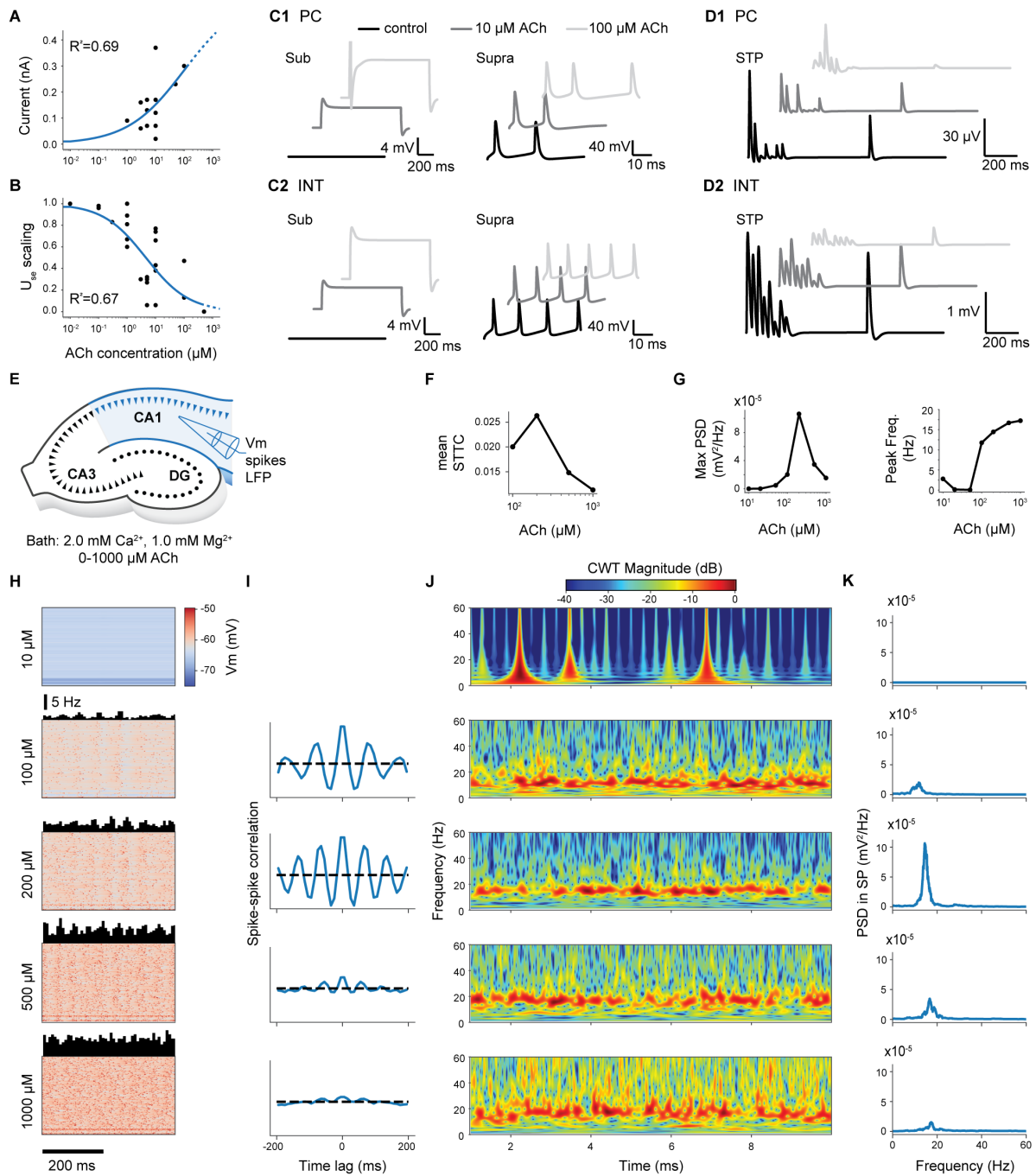411 the effects of other neuromodulators.

Figure 5: **Acetylcholine modeling**. *(for legend, see next page)*

Figure 5 *(previous page)*: **Acetylcholine modeling**. A. Dose-response modulation of neuronal excitability caused by ACh. Experimental data points (black dots) are extracted from the literature and the blue curve represents the fitted equation describing the relationship between ACh concentration (in µM) and the depolarizing current (in nA). The dashed part of the curve indicates regions outside available experimental data. B. Dose-response modulation of synaptic release. Same as in A, but describing the relationship between the ACh concentration and the scaling of the U_{SE} parameter (adimensional). C. Example traces for PC (C1) and interneurons (C2) in sub-threshold and supra-threshold conditions, with different concentrations of ACh (control: black, $10\,$µM: dark gray, and $100\,$µM: light gray). D. Example traces showing the STP dynamics for PC (D1) and interneurons (D2) at different concentrations of ACh. E. The illustration shows the *in silico* experimental setup to analyze network effects of CCh. Different concentrations of CCh are applied to the circuit, and multiple types of recordings made in the CA1 (membrane voltage, spike times, LFPs). F. The voltage of 100 randomly selected neurons during 500 ms of simulation at different levels of ACh. The upper histograms show the instantaneous firing rate (in bins of 10 ms). G. Mean spike time tiling coefficient (STTC) values computed for 10,000 pairs of CA1 neurons with spike trains lasting 9 s as a function of CCh concentration. H. Spike-spike correlation histograms (bin $=$ 10 ms) computed for 10,000 pairs of CA1 neurons. I. LFP measured in SP computed in simulations at four different ACh levels. Colors correspond to different levels of continuous wavelet transform (CWT). J. PSD of the LFPs reported in panel I. K. Maximum of the LFP power spectrum density (PSD, in mV^2 Hz^{-1}) and location of the peak frequency (in Hz) as a function of ACh concentration.

2.2 Model simulation and applications

In this section, we explain how to use the model to set up simulation experiments, accurately replicate experimental setups, and address scientific questions. A simulation experiment is essentially a model of the experimental setup that is reproduced with as much accuracy as possible. As presented in the reconstruction section, the model contains features that allow us, for example, to make slices of a certain thickness, change extracellular concentration of ions, change temperature, and enable spontaneous synaptic events. Here, we show several simulations with particular emphasis on theta oscillations, a prominent network phenomenon observed in the hippocampus *in vivo* and related to many behavioral correlates (Buzsáki, 2005). Despite extensive research on hippocampal theta oscillations, the scientific community has yet to converge on a single model, and conflicting evidence remains. However, this represents an opportunity to use the model to integrate existing knowledge into a coherent framework. Additionally, the model also allows us to explore many different ramifications of the initial scientific question. Following one of these ramifications, in the second part of the simulation section, we go beyond the theta oscillations and test whether a wider range of frequencies can pass more reliably through SC than other pathways.

2.2.1 Theta oscillations

During locomotion and REM sleep, CA1 generates a characteristic rhythmic theta-band (4-12 Hz) extracellular field potential (Goyal et al., 2020; Grastyan et al., 1959; Green & Arduini, 1954; Jung

430 & Kornmüller, 1938; Vanderwolf, 1969). Neurons in many other brain regions such as neocortex are
431 phase-locked to these theta oscillations (Siapas et al., 2005; Sirota et al., 2008) suggesting hippocampal
432 theta plays a crucial coordinating role in the encoding and retrieval of episodic memory during spatial
433 navigation (Buzsáki, 2002, 2005). The activity in each of the different classes of CA1 neurons correlates
434 with specific phases of the theta cycle suggesting a complex interaction between pathways (see Table
435 S22): pyramidal cells, OLM, and BS spike during the rising phase, CCKBC and AA discharge before or
436 at the peak, and PVBC fire in the falling phase of the theta cycle (Fuentealba et al., 2008; Klausberger,
437 2005; Klausberger et al., 2003, 2004).

438 Yet despite more than eighty years of research, the trigger that generates theta oscillations in CA1
439 remains unclear. *In vivo* evidence points to a fundamental role of the medial septum (MS) (Colgin, 2013).
440 MS contains hyperpolarization-activated cyclic nucleotide–gated channel (HCN)-expressing interneurons
441 that fire rhythmically at theta frequencies and are phase-locked to theta rhythms in the hippocampus
442 (Hangya et al., 2009). These cells are believed to target CA1 interneurons preferentially (Sun et al.,
443 2014). GABAergic MS interneurons predominantly target parvalbumin-positive (PV+) interneurons
444 in CA1 offering a disinhibitory mechanism for theta generation (Müller & Remy, 2018; Sun et al.,
445 2014). Depth recordings in CA1 have identified two main extracellular current sink-source current for
446 theta rhythms (Brankack et al., 1993; Kamondi et al., 1998; Kocsis et al., 1999). The strongest active
447 current sink is located in SLM, where perforant path (PP) input terminates (Kamondi et al., 1998; Ylinen
448 et al., 1995). The weaker active source-sink is located between SR, where associational and commissural
449 CA3 axons terminate, and SP, where perisomatic inhibition of pyramidal cells occurs. The cholinergic
450 antagonist, atropine, can block theta when the PP pathway is bilaterally removed but theta is largely
451 unaffected when it is intact (Ylinen et al., 1995), suggesting the existence of independent atropine-
452 resistant and atropine-sensitive theta oscillation generators. More recently, an intrinsic generator has
453 been considered. Goutagny et al. (2009) recorded spontaneous atropine-resistant theta oscillations in
454 an *in vitro*, intact, isolated, mouse hippocampal preparation but not in horizontal or transverse slices
455 prepared from the same tissue. While the amplitude was 10-20% of that *in vivo* (Goutagny et al.,
456 2009), these theta oscillations were abolished when $GABA_A$ receptors were blocked suggesting that an
457 interaction between local pyramidal cells and interneurons might contribute to theta generation.

Intrinsic generation

459 To investigate possible intrinsic mechanisms of theta rhythm generation in CA1 (Goutagny et al., 2009),
460 we examined three candidate sources of excitation that might induce oscillations: (i) spontaneous
461 synaptic release or miniature postsynaptic potentials (minis or mPSPs), (ii) homogeneous random spiking
462 of SC afferent inputs, and (iii) varying bath concentrations of extracellular calcium and potassium to
463 induce tonic circuit depolarisation. While in their CA1 circuit model Bezaire et al. (2016) reported
464 random synaptic activity was sufficient to induce robust theta rhythms, in our model we found none
465 of these candidates generated robust theta rhythms. For minis, we found setting release probabilities
466 to match empirically reported mPSP rates (Table S21) led to irregular, wide-band activity in CA1 (see
467 Figure S17). For random synaptic barrage, varying presynaptic rate to match the mean postsynaptic
468 firing rate of pyramidal cells in Bezaire et al. (2016) resulted in irregular beta-band not regular theta-
469 band oscillations (see Figures S18 and S19). Meanwhile, for tonic depolarisation, within a restricted

470 parameter range it was possible to generate theta oscillations around 10-12 Hz, but their intensity was
471 variable and episodic (see Figures S20 and S21).

Extrinsic pacemakers

473 After investigating possible intrinsic mechanisms, we examined whether theta oscillations could be
474 generated by extrinsic oscillatory sources such as CA3 or by disinhibition via medial septum (MS)
475 GABAergic projections.

CA3 input

477 To mimic the influence of CA3 theta oscillations in CA1, we generated spike trains in a random subset of
478 SC axons that were modulated by a sinusoidal rate function with signal frequency (range 4-10 Hz) and
479 inhomogeneous random Poisson spike times for a range of mean individual SC axon spiking rates (0.1-0.4
480 Hz). As Goutagny et al. (2009) found that the volume of isolated hippocampus *in vitro* was crucial to
481 whether theta oscillations were generated or not, we compared simulations performed at different scales
482 using whole circuit, thick slice circuit, and cylinder microcircuit models (Figure 2).

483 Across all scales of circuit tested, for *in vitro* calcium levels ($2\,\mathrm{mM}$) the LFP signal faithfully reproduced
484 the modulation frequency of the sinusoidal input signal in theta-band. For example, 8 Hz modulated
485 spike trains delivered via SC axons generated a highly regular 8 Hz LFP signal in CA1 full, thick slice
486 and cylinder circuit models (Figure 6ABC). In rat CA1, theta oscillation waveforms are typically more
487 sawtooth-like than sinusodial (Buzsáki et al., 1985). Waveform asymmetry can be described using the
488 asymmetry index, which is the log ratio of the duration of the rising and decaying phases of the LFP
489 oscillation, e.g. in rats the mean index is -0.27 during locomotion and -0.13 during REM sleep periods
490 (Belluscio et al., 2012). Here we found the generated LFP waveforms were highly asymmetrical with a
491 fast rise and slower decay (mean asymmetry index $= -1.34 \pm 0.23$; see Figure S22). A strong narrow-
492 band peak of power at 8 Hz was maintained throughout the entire period of stimulation (Figure 6ABC,
493 middle columns). Consistent with experimental evidence (e.g. Figure 1b in Goutagny et al., 2009),
494 first (16 Hz) and second order (24 Hz) harmonics of the theta modulation frequency were also present.
495 The magnitude of the modulation and harmonic powers were directly proportional to circuit size (Figure
496 6ABC, middle right column). Current source density (CSD) showed a highly regular alternating current
497 dipole between layers with a phase reversal between stratum pyramidale and stratum radiatum, similar
498 to *in vivo* LFP recordings in the absence of perforant pathway input (Figure 6ABC, far right column).
499 However, at *in vivo* calcium levels ($1\,\mathrm{mM}$), while the full circuit showed similar frequency response, it
500 was around three orders of magnitude less powerful due to the far lower CA1 spiking rate (e.g. in full
501 circuit, pyramidal cell mean firing rate of 0.00018 ± 0.0067 (1 mM) vs 0.25 ± 0.50 Hz (2 mM); Figure
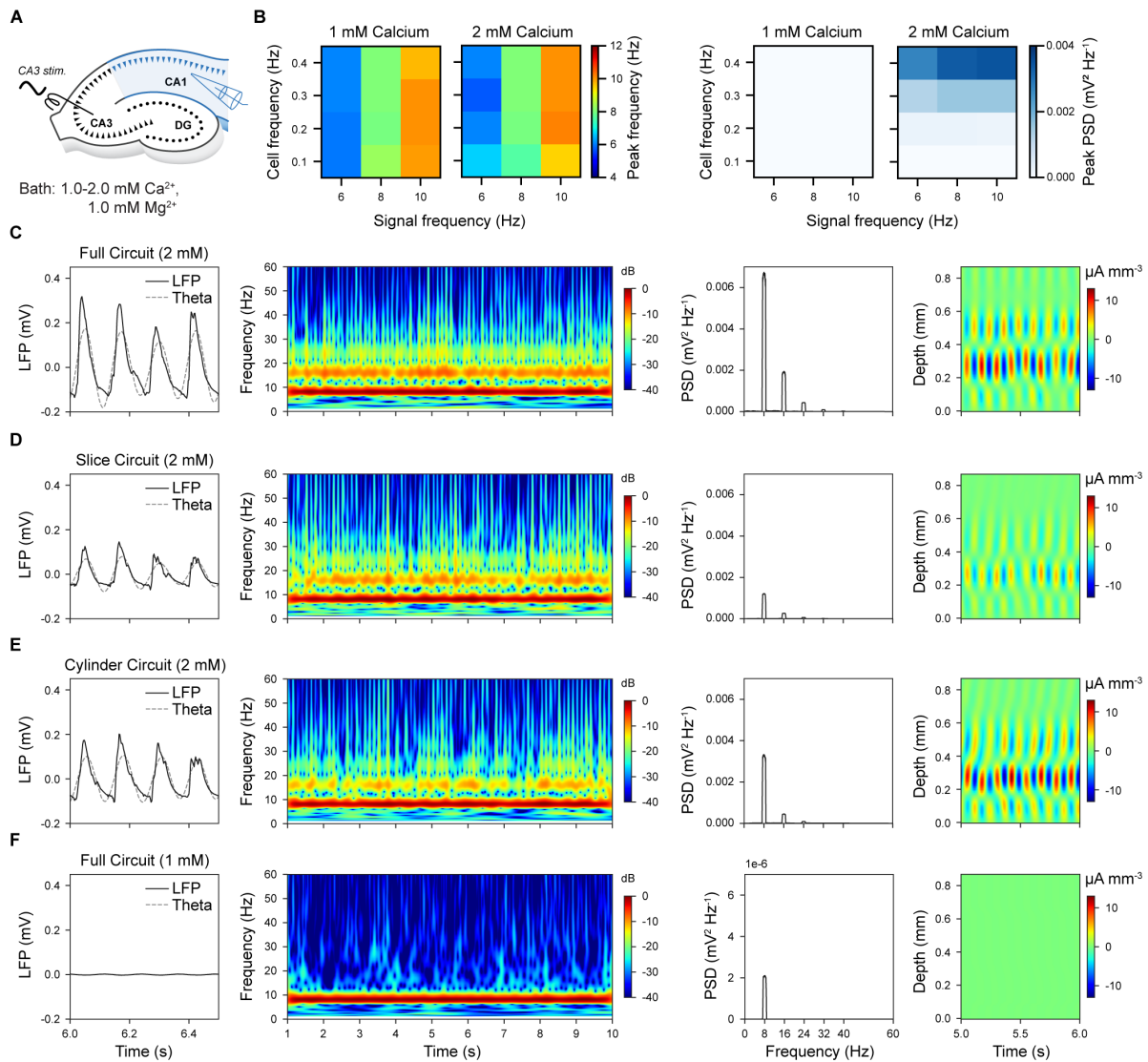502 6D).

Figure 6: **CA3 theta (8 Hz) oscillatory input entrains CA1 to matched theta oscillation across different scales of circuit**. *(for legend, see next page)*

Figure 6 *(previous page)*: A. Full circuit model (2 mM calcium). B. Slice circuit model (thickness of 300 µm, 2 mM calcium). C. Cylinder circuit model (radius of 300 µm, 2 mM calcium). D. Full circuit model (1 mM calcium). Far left column, extracellular LFP recordings from stratum pyramidale (SP) show highly regular but asymmetric shape waves at 8 Hz. Left middle column, the Morlet complex wavelet spectrogram shows constant 8 Hz energy with first and second order harmonics present. Right middle column, power spectral density (PSD) shows identical qualitative power distribution independent of circuit scale while magnitude is in direct proportion to circuit size (N.B. panel D has 1000 times smaller y-axis scaling than panels ABC). Far right column, current source density (CSD) analysis of translaminar currents showing stratum pyramidale and stratum radiatum current dipoles alternating at 8 Hz.

503   When the spike times of neurons close to the extracellular recording electrode in stratum pyramidale were

504 compared with the phases of theta-band LFP rhythm (theta trough = 0°), all neuron types were found
505 to respond at roughly the same phase of the theta cycle (Figure 7). In a cylinder circuit, for example,
506 as the mean rate of SC afferent spiking increased more neurons became phase-locked yielding a denser
507 mono-phase distribution for higher signal modulation frequencies (Figure 7A). For example, under stimuli
508 with a 0.4 Hz SC mean spiking frequency and 8 Hz signal modulation, CA1 pyramidal cells fired first
509 during the mid-rising phase and were followed by all types of interneurons, whose spiking mostly ended
510 before peak theta, with bistratified neurons emitting few or no spikes (Figure 7B left). Significantly
511 phase-locked neurons had tighter tuning with pyramidal-interneuron phase-ordering (Figure 7B middle).
512 When compared with *in vivo* recordings of phase-locked neurons (see Table S22) (Fuentealba et al.,
513 2008; Klausberger, 2005; Klausberger et al., 2003, 2004), the mean phase angle of model spiking was
514 closely matched for CCK+ basket cells but substantially out of phase for axoaxonic cells (Figure 7B
515 right). Although the angular deviation of phase-locking was generally tighter than observed *in vivo*
516 (e.g., model vs *in vivo* for SP_AA 8.9°(n=4) vs 55.0°(n=2), SP_PVBC 12.0°(n=2) vs 68.0°(n=5), and
517 SP_Ivy 10.9°(n=19) vs 63.1°(n=4)).
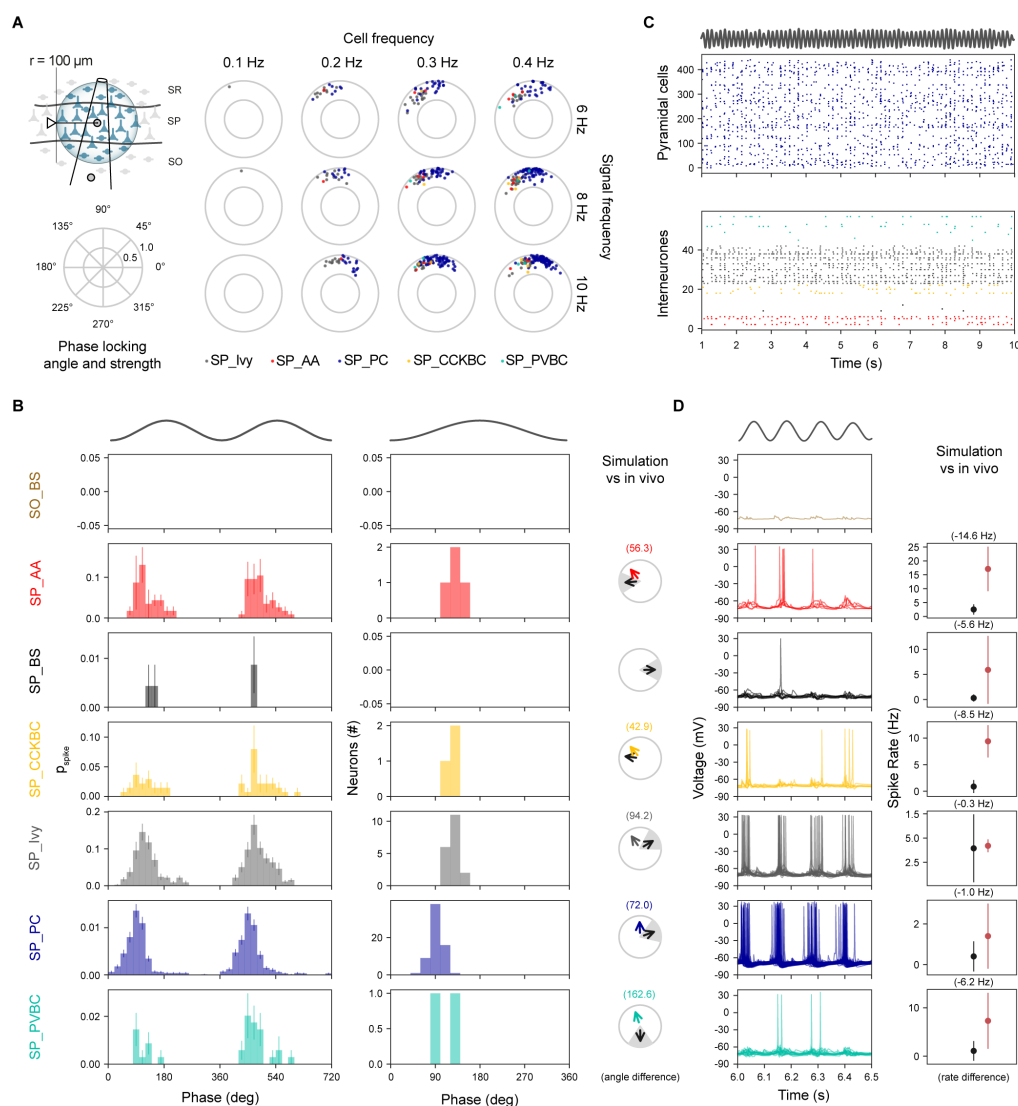
Figure 7: **CA1 morphological types are homogeneously tuned to CA3 theta oscillatory input**.*(for legend, see next page)*

23

Figure 7 *(previous page)*: A. Phase locking angle and strength for a range of individual SC cell frequencies (columns) and modulation frequencies (rows) shows a single grouping. Neurons for analysis were selected within $100\,\mu$m radius of the stratum pyramidale electrode location. B. Phase Modulation. Left: Spike discharge probability of all neurons grouped by morphological type shows they tuned between mid-rising phase and peak of theta LFP rhythm with SP_PC slightly in advance of interneurons. Middle: phase locked neurons tuning over theta cycle for each morphological class over a single theta cycle is tighter but with the grouping preserved. Right: Experimental validation of phase-locking generally shows poor match to *in vivo* recordings. C. Spiking raster plots over many seconds show strong phase modulated SP_PC cell spiking (top panel) compared with LFP theta rhythm (trace above plot) with intereuron spiking (bottom panel) of SP_Ivy cells showing a similar spiking pattern but other interneurons spiking fired more irregularly. D. Intraceullar traces from morphological cell types. Left: SP_PC and SP_Ivy cells spiking responses were similar, although firing in SP_Ivy cells was relatively delayed. The firing of other interneuron types overlaps with that of SP_Ivy cells. Right: All neuronal types except SP_Ivy cells are less active than *in vivo* during theta rhythms with SP_Ivy and especially SP_AA types outside the range recorded in *in vivo*.

518 For *in vitro* calcium levels (2 mM), pyramidal cell spiking was closely aligned to theta LFP rhythm
519 although individual neurons did not spike at every cycle (Figure 7C top). Ivy cells showed a similar
520 pattern to pyramidal cells while other types of interneuron participated more sporadically (Figure 7C
521 bottom). Intracellular voltage traces for pyramidal and ivy cells were also similar albeit with ivy cell
522 firing slightly later and overlapping with other types of interneurons (Figure 7D left). Mean firing rates
523 during theta were generally lower than observed *in vivo* except for ivy cells, which was a close match;
524 axoaxonic, bistratfied, and basket cells (CCK+ and PV+) were well below empirical expectations (Figure
525 7D right). During 8 Hz theta, the pyramidal cell membrane potential was modulated by 1.57-7.34 mV
526 (for 0.1-0.4 Hz SC axon frequency), consistent with the *in vivo* range (2-6 mV, Ylinen et al., 1995).
527 When we compared model population synchrony during theta oscillations with *in vivo* data (Csicsvari
528 et al., 1998), we found that, regardless of circuit size, the percentage of pyramidal cell spiking was a
529 poor match around the theta trough (0°) but was a better match around theta peak (180°), while fast-
530 spiking PV+ basket cells and to a lesser degree axoaxonic cells were under-recruited (see Figure S23).
531 Overall, for this stimulus the pyramidal-interneuron theta phase order suggests that intrinsic inhibition
532 was activated more powerfully by recurrent than by afferent excitation.

Medial septum input

534 Medial septum (MS) has for many decades been considered a main generator of CA1 theta rhythms
535 (Colgin, 2013). In the absence of a detailed model of MS cholinergic and GABAergic projections to CA1,
536 we attempted to reproduce its *in vivo* effects by (i) setting an *in vivo* extracellular calcium concentration
537 (1 mM), (ii) applying a tonic depolarizing current (% of rheobase current) to all neurons to represent
538 *in vivo* background activity, (iii) introducing an additional current to mimic the depolarizing effect of
539 an arhythmic release of ACh from the cholinergic projection (see ACh section), and (iv) applying a
540 theta frequency sinusoidal hyperpolarizing current stimulus only to PV+ CA1 neurons to represent the
541 rhythmic disinhibitory action of the GABAergic projection (see Figure 8A).

Prior to the onset of the disinhibitory stimulus ("MS OFF"), the global tonic depolarization resulted in weak, irregular beta-band LFP activity in CA1 but after its onset ("MS ON"), it induced a strong and sustained, regular theta oscillation matching the frequency of the hyperpolarizing stimulus (see Figure 8B). The LFP waveforms generated were close to symmetrical (mean asymmetry index $= 0.25 \pm 0.11$; see Figure S24). Over a range of ACh concentrations and tonic depolarization levels, this theta rhythm was robust, narrow-band (Figure 8BC), and was generated by a highly regular current source restricted to stratum pyramidale (Figure 8E). Higher ACh concentrations, while slightly reducing theta-band power, reduced the level of beta-band activity (Figure 8C). Increased levels of tonic depolarization enhanced theta harmonics and higher frequency components (Figure 8CD). Theta-band power was more dependent on the amplitude of the disinhibitory oscillation than either ACh concentration or tonic depolarization level (Figure 8F).
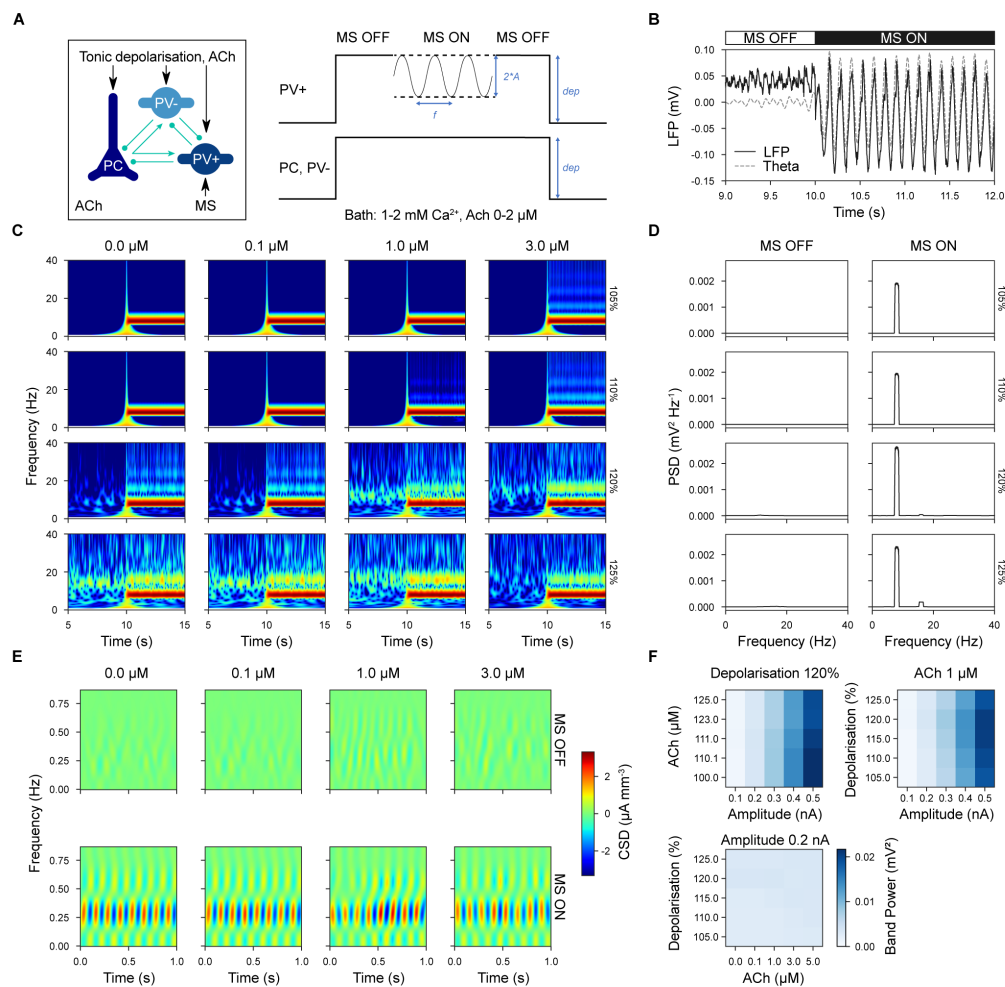
Figure 8: **Medial septum (MS) disinhibition of parvalbumin-positive (PV+) interneurons induced theta oscillations in CA1**. *(for legend, see next page)*

25

Figure 8 *(previous page)*: A. In this setup, all neurons received a tonic depolarizing current as a percentage of each neuron's rheobase current only ("MS OFF" condition) and later, for a given period an oscillatory hyperpolarizing current was injected into PV+ interneurons only ("MS ON" condition) in the presence of ACh. B. Before onset of disinhibition ("MS OFF"), CA1 showed weak, irregular beta-band activity but changed to strong, regular theta-band activity after onset of disinhibition ("MS ON"). C. Morlet complex wavelet spectrogram shows how efficiently dishinibition induces theta oscillations throughout the oscillatory period and for range of ACh concentrations and tonic depolarisation levels following onset of disinhibition. D. Power spectral density (PSD), across different levels of tonic depolarization, exhibits an absence of any strong theta response without disinhibition, but narrow-band 8 Hz with disinhibition. E. Current source density (CSD) analysis shows lack of a strong oscillation across layers before the oscillatory disinhibitory stimulus (top) but a strong source-sink alternation in stratum pyramidale ($\sim$0.3 mm depth) during the stimulus (bottom). F. Theta band power was more dependent on the amplitude of oscillatory hyperpolarizing current than ACh concentration or level of tonic depolarization.

During theta rhythm, morphological cell type responses separated into one of two main groups that were in anti-phase with each other (see Figure 9). As the level of tonic depolarization increased, more phase locked cells were detected (Figure 9A) and only above 110% depolarization (where 100% represents the depolarization necessary to reach spike threshold) were there enough interneurons, that were active enough to discern this dual grouping. Increasing ACh concentration tended to weaken pyramidal phase locking (Figure 9A). For example, at 120% depolarisation and 1 μM ACh, the firing of pyramidal, ivy, and CCK+ basket cells was broadly tuned around the theta trough and rising phase, while the firing of axoaxonic, bistratified and PV+ basket neuron was more narrowly tuned around the peak of the theta rhythm (Figure 9B left). Neurons with significant phase locking matched this pattern but were even more narrowly tuned (Figure 9B middle). The phase locking of axoaxonic, ivy and pyramidal cells closely matched *in vivo* recordings (see Table S22) (Fuentealba et al., 2008; Klausberger, 2005; Klausberger et al., 2003, 2004) but bistratified and basket cells (CCK+ and PV+) were by comparison more than 90 degrees out of phase (Figure 9B right).
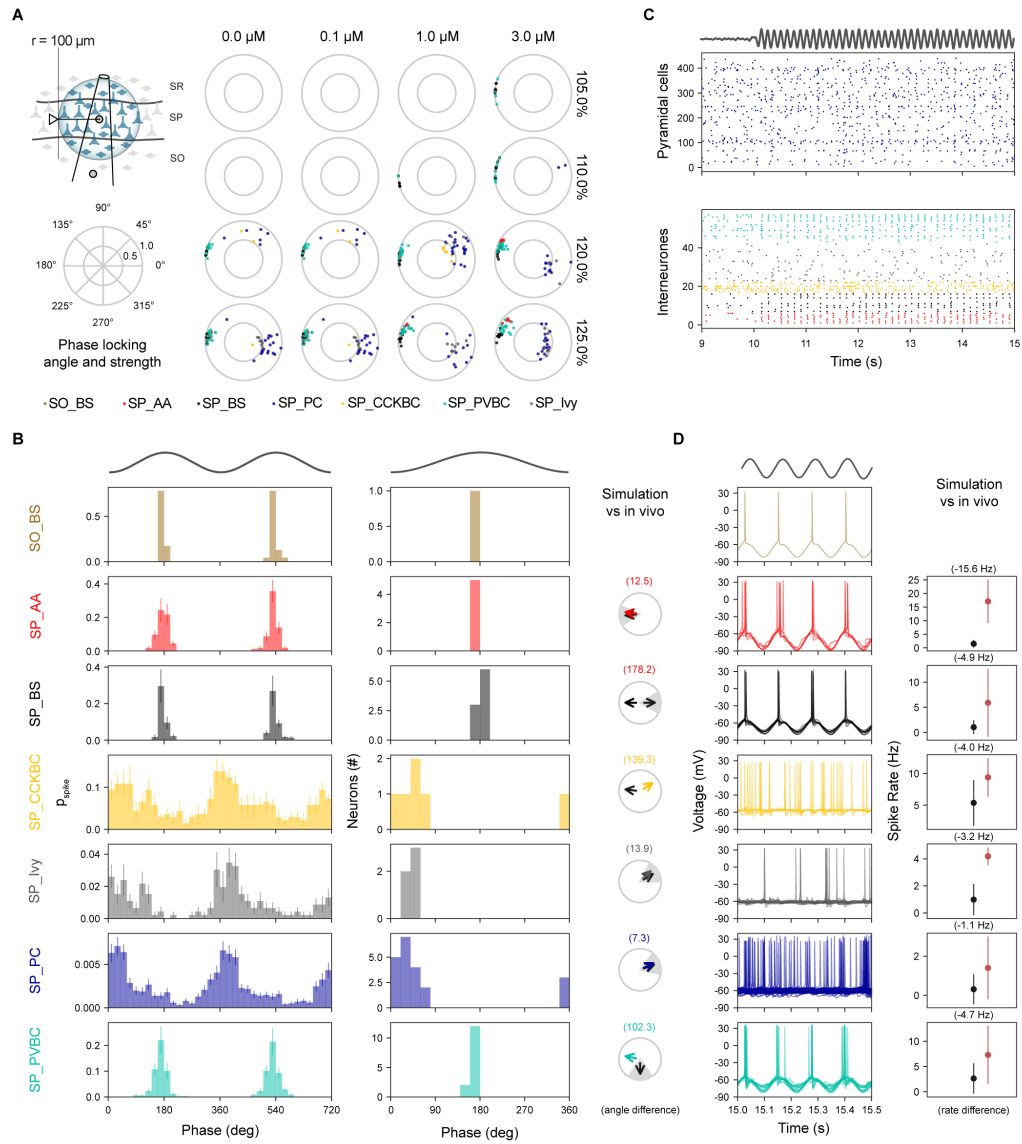
Figure 9: **Medial septum (MS) disinhibition induced anti-phase modulation of CA1 neurons during theta cycles**.*(for legend, see next page)*

Figure 9 *(previous page)*: A. Phase locking angle and strength for range of ACh concentration (columns) and levels of tonic depolarization (where 100% represents the spike threshold, rows) for modulation amplitude (A=0.2 nA) divides cell types into two groups (SP_PC grouped with SP_Ivy and SP_CCKBC, while SP_PVBC grouped with SO_BS, SP_AA, and SP_BS) once enough phase-locked interneurons of each type are included. Neurons for analysis were selected within $100\,\mu m$ radius of the stratum pyramidale electrode location. B. Phase Modulation. Left: Spike discharge probability of all neurons grouped by morphological type shows PV+ neurons (SO_BS, SP_AA, SP_PVBC, and SP_BS) are closely tuned to peak of LFP theta-band (top trace) while pyramidal cells and PV- interneurons (SP_CCKBC and SP_Ivy) are more broadly tuned around theta trough (0°). Middle: Phase locking for each morphological class over a single theta cycle is tighter than reported experimentally especially PV+ interneurons. Right: Experimental validation of phase locking shows some cell types closely match *in vivo* recordings (SP_AA, SP_Ivy and SP_PC) while others are more than a quarter-cycle out of phase (SP_BS, SP_CCKBC and SP_PVBC). C. Spiking raster plots over longer period show weaker phase modulation in pyramidal cell spiking (top panel) than in LFP theta rhythm (trace above plot). PV+ interneurons are tightly modulated, however, while PV- interneurons are more weakly modulated (bottom panel). D. Intraceullar traces of morphological cell types. Left: PV+ interneurons tightly spike on release from disinhibition whereas PV- interneurons do not. Right: comparing firing rates, all neuronal types in the model are less active than *in vivo* during theta rhythms with SP_Ivy and especially SP_AA types outside empirical range.

566 At first sight, the pattern of pyramidal firing appears to be more weakly modulated by theta but
567 pyramidal cells failed to spike on every theta cycle (Figure 9C top). In contrast, whereas axoaxonic,
568 bistratified, and PV+ basket cells spiked tightly for most cycles, ivy cells spiked more rarely and CCK+
569 basket cells more tonically (Figure 9C bottom). Intracellular voltage traces for axoaxonic, bistratified,
570 and PV+ basket cells showed they spiked tightly on the rebound from the release of the hyperpolarizing
571 stimulus, whereas pyramidal and other interneurons lacking this were less reactive to theta (Figure
572 9D left). However, all neurons spiked at a lower average rate than *in vivo* recordings (Fuentealba
573 et al., 2008; Klausberger, 2005; Klausberger et al., 2003, 2004) with pyramidal cells around 1 Hz
574 lower and, at the extreme, axoaxonic cells almost 16 Hz lower (Figure 9D right, stimulus: modulation
575 amplitude 0.2 nA, 120% depolarization and $1\,\mu M$ ACh). The population synchrony of pyramidal cells
576 with theta trough ("theta-") was consistent with *in vivo* data (Csicsvari et al., 1998) for a range of
577 disinhibitory stimulus amplitudes whereas for fast-spiking interneurons like axoaxonic and PV+ basket
578 cells, synchronization with theta peak ("theta+") only occured with lower stimulus amplitudes (Figure
579 S25). Overall, the network response to an extrinsic, inhibitory, oscillatory stimulus matched many though
580 not all experimental validations of *in vivo* theta oscillations in CA1.

581 Taken together, the simulations showed the interplay between extracellular calcium concentration, tonic
582 depolarization, ACh, and MS disinhibition. ACh and depolarization cooperate to increase excitability.
583 Similarly, both ACh and low extracellular calcium concentration tend to decouple the neuron activity. The
584 latter prevents the higher-frequency oscillation that otherwise results from the depolarization. Instead,
585 it generates sparse activity necessary to entrain the network to the rhythm imposed by MS disinhibition.

In summary, we investigated five possible mechanisms for theta oscillations compatible with a variety of experimental setups: (i) spontaneous synaptic release, (ii) random afferent synaptic barrage, (iii) bath manipulation of calcium and potassium, (iv) excitatory oscillatory input via Schaffer collaterals, and (v) oscillatory disinhibition via medial septum GABAergic projections. Spontaneous synaptic release and random afferent synaptic barrage did not induce detectable theta oscillations in the model. Tonic depolarization at certain strengths induced a variable and unstable theta oscillation at 10-12 Hz. More stable and stronger theta oscillations followed extrinsic drivers. Importantly, while the model showed that both inputs trigger theta, the underlying mechanisms were different, and effect of MS disinhibition was more compatible with *in vivo* data. The presence of multiple mechanisms could explain, at least in part, the heterogeneity of the experimental data.

2.2.2   Propagation of oscillatory inputs

As illustrated above, an oscillatory input through SC can reliably produce an oscillation of the same frequency in CA1 (see section onTheta oscillations). To test whether other input frequencies (i.e., 0.5-200 Hz) applied via SC afferents also reliably entrained oscillations of the same frequency in CA1, we simulated an oscillatory input from CA3, with four different signal strengths (i.e., changing the average firing rate of CA3 PC: 0.1 Hz, 0.2 Hz, 0.4 Hz, and 0.8 Hz) and measured the activity of CA1 (Figure 10A).

The I-O gain, minimally defined as the ratio between the overall number of output spikes divided by the number of input spikes, is not constant, but it depends both on the mean firing rate of CA3 PCs and on the oscillatory frequency of the input (Figure 10B). For each CA3 mean firing rate, the number of output neurons is maximized at different frequencies. Notably, the I-O responses of PC and interneurons are radically different (Figure 10B). Overall, the highest CA1 output was obtained with a 0.4 Hz mean CA3 frequency. For this reason, we considered this condition for further analysis.

I-O responses of CA1 displayed band-pass filtering characteristics. Focusing on spike train correlations (examples of spike trains in Figure 10C), CA1 activity is generally well correlated with the input from CA3 for delta to low gamma input frequencies (i.e., between 1 and 30 Hz), while for lower and higher frequencies the correlation decreases. A similar pass-band filtering behavior can be seen in the internal CA1-CA1 spike time tiling coefficient (STTC). In this case the pass-band bandwidth is larger, extending to the gamma band (Figure 10D). The spike-spike correlation histograms confirm the propagation of oscillations from CA3 to CA1 for delta to gamma waves (Figure 10E). All spike train correlation measurements have been repeated using standard covariance and cross-correlation functions, and they confirmed the results obtained with the STTC analysis (not shown).
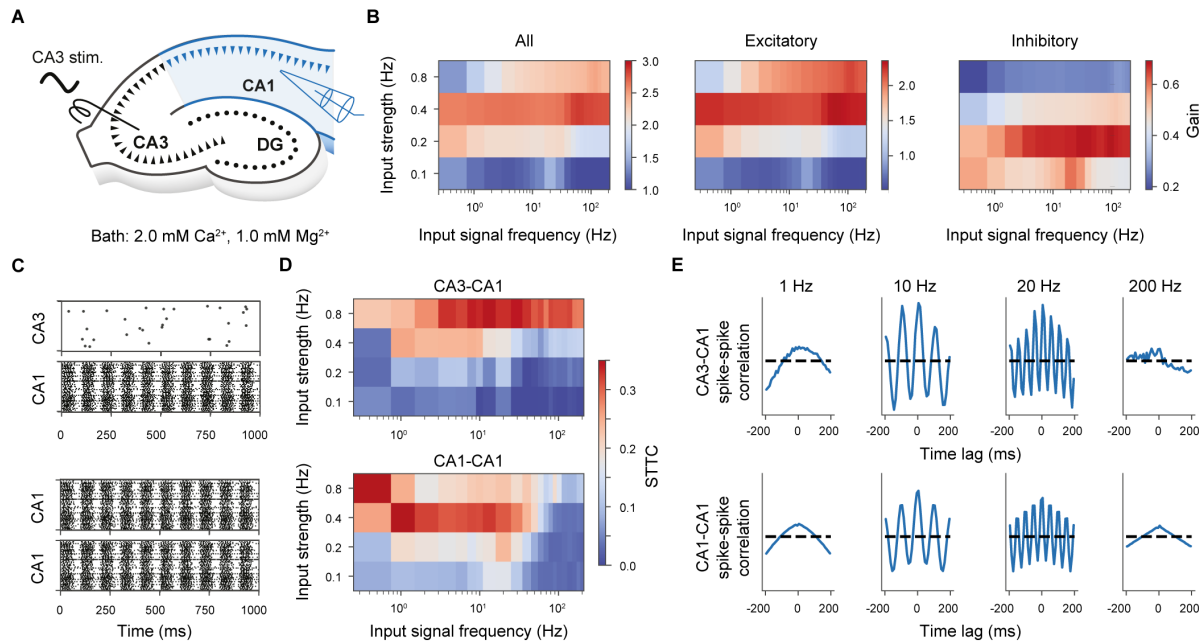
Figure 10: **I-O transformation**. A. The illustration shows the *in silico* experimental setup used to study the propagation of CA3 oscillations in CA1. B. Ratio between the number of CA1 (output) and CA3 (input) spikes as a function of the input oscillation frequency (abscissae) for four levels of input mean firing rate (ordinatey-axis). Considering all CA1 neurons (left) or uniquely CA1 PCs (center) and CA1 interneurons (right). C. Examples of CA3 and CA1 spike train (in this case for 0.4 Hz mean CA3 firing rate and oscillation frequency of 10 Hz). 100 random CA3 neurons and CA1 neurons are selected and shown. The same neurons are used to compute the 10,000 pairs of STTC and spike-spike correlations (panels D-E), in one case crossing CA3 and CA1, in the other case within CA1 neurons. D. Heatmaps representing the computed STTC values (bins $= 10$ ms) for each combination of input oscillation (abscissae) and mean CA3 frequency (ordinate), for CA3-CA1 and CA1-CA1 neurons, respectively. E. Spike-spike normalized correlation histograms (bins $= 10$ ms, 1 s of simulated activity) in four example cases: 1 Hz, 10 Hz, 20 Hz, and 200 Hz (with a mean CA3 firing rate of 0.4 Hz), for CA3-CA1 and CA1-CA1 neurons, respectively.

To determine whether particular experimental conditions might have an impact on the result, we specifically selected a study examining gamma-band oscillations *in vitro* (Zemankovics et al., 2013). We analyzed the local field potential in the CA1 network model while it was driven by SC input modulated at gamma frequency. The properties of this external drive and simulation conditions were exactly tailored to these *in vitro* experiments (e.g. $300\,\mu$m-thick slices, $2\,$mM extracellular Ca^{2+}, $2\,$mM extracellular Mg^{2+}, $10\,\mu$M ACh). As the present circuit does not model the topography of SC connections to CA1 neurons, it does not constrain how many active SCs project to the simulated slice. Therefore, we ran multiple simulations varying the number of activated SCs, from none to all. We observed that gamma oscillatory SC input could entrain the entire CA1 network of the model slice to oscillate at the driving frequency (31 Hz) (Figure S26A). In the experiment of Zemankovics et al. (2013), the authors added carbachol (CCh) to generate oscillations in CA3, which were transmitted to CA1 via SC, but it is not clear whether CCh also has a significant effect on CA1 at the concentration used in the experiment. To quantify the effect of CCh, we reran the simulation without CCh. SC inputs, ranging from 15,000 to

631 100,000, were able to induce strong gamma oscillation in the absence of CCh. However, CCh increased
632 the number of inputs needed for stable gamma oscillation, probably due to its weakening effect on
633 synapses (Figure S26B).

634 Oscillations at several frequencies can be induced in CA3 and reliably transmitted to CA1 *in vitro*
635 (Bianchi & Wong, 1994; Fellous & Sejnowski, 2000; Fisahn et al., 1998; J. H. Williams & Kauer,
636 1997). Sasaki et al. (2006) also showed that the CA1 network responded more reliably in the near-
637 gamma frequency (20-40 Hz) range, acting like a band-pass filter. Other frequencies (e.g., ripples) are
638 generated locally in CA1 and are not driven by CA3 activity (Buzsáki, 2015). Our model confirmed
639 the CA1 network could be entrained into an oscillatory behavior at various frequencies, by CA3 inputs.
640 However, input frequencies that are either too low (< 1 Hz) or too high (> 100 Hz) input frequencies
641 fail to propagate. This implies that intermediate frequencies can be used efficiently to synchronize CA1
642 with other brain regions or to carry information to CA1. The I-O relationship in different conditions
643 changes non-linearly as a function of both the input oscillatory frequency and its strength. Finally, our
644 results show that CCh does not significantly influence the propagation of gamma oscillation from CA3
645 to CA1 and suggest that the main effect of CCh is the generation of gamma oscillation in CA3.

3 Discussion

3.1 Main summary

This study presents the reconstruction and simulation of a full-scale atlas-based model of the rat hippocampal CA1 region driven by community data and collaboration. We extended and improved the framework of Markram et al. (2015) to curate and integrate a wide variety of anatomical and physiological experimental data from synaptic to network levels. We then systematically applied multiple validations for each level of the model. We augmented the resulting highly detailed intrinsic CA1 circuit with a reconstruction of its main input from CA3 and a phenomenological model of neuromodulation by acetylcholine. Importantly, the circuit model is general and not created to reproduce a narrow spectrum of use cases but to be capable of addressing a wide range of research questions. To demonstrate its general utility, we were able to simulate different scales of circuits and investigate the generation and transmission of neuronal oscillations, with particular emphasis on theta rhythm, for a variety of stimulus conditions.

3.2 Previous work and limitations

For more than three decades, there has been a progression in both the size and level of detail of large-scale multiscale models of the rat hippocampus (for a comparison of their key features with the present model, see Table S2). These biologically realistic models aim to explain the complex dynamics of hippocampal activity, in particular the generation and control of rhythmic responses. However, none of these models, including the one reported here, provides a complete description of a hippocampal region or regions. Moreover, the results of these models are difficult to compare because of fundamental differences in their composition, organization, and underlying assumptions.

The current model stands out as the only model that realistically constrains the neurons and their connectivity by the highly curved shape of CA1 rather than by an artificial space and that reflects short-term plasticity and spontaneous synaptic release, both well-established characteristics of central nervous system synapses. In addition, the morphologies and electrical properties of model neurons here are not just copies of the same class exemplars but their properties have been systematically varied to better capture the diverse nature of neuronal circuits and their responses to stimulation. However, compared with Bezaire et al. (2016), some elements are still missing from the current model such as neurogliaform cells, which did not exist in our available dataset, and $GABA_BR$ which are not included in our simulations.

Nonetheless, the current model includes the perforant path-associated (PPA) and trilaminar interneurons, which were absent from all previous models. In addition, we modeled the NMDA synaptic currents observed in both hippocampal pyramidal cells and interneurons (with specific NMDAR conductance, rise and decay time constants for each pathway) that are absent in the model of Bezaire et al. (2016). Furthermore, the connectivity algorithm used for the current model generates an intrinsic connectome with more realistic high-order statistics than the more prescriptive approach used in the Bezaire et al. (2016) model (Giacopelli et al., 2021). Unlike Yu et al. (2020), we did not replicate the topography of the afferent projections, which may play a role in patterning the circuit response, but did model the projections and circuit at a full rather than reduced scale. Overall, further improvement to our model

32

685 requires additional experimental data.

686 While we incorporated key features distributed among previous models into a single, general model (see
687 Table S2), it is important to recognise that our aims and approach were different, representing a step
688 change in hippocampal modeling. The intention of the framework was first to curate and integrate
689 community data into the model, preserving provenance for reproducibility, in a way that would allow
690 the addition of new datasets from the large hippocampal community. Re-using these datasets and
691 then making them publicly available through hippocampushub.eu supports the 3R principles (replace,
692 reduce, refine) for the reduction of animal experiments. Each circuit component and the final model
693 was then systematically validated in an open and transparent way to a degree not previously attempted.
694 To increase the realism and utility of simulation experiments, we sought to approximate experimental
695 conditions (e.g. slice thickness and location, bath calcium, magnesium and acetylcholine concentrations,
696 and recording temperature) and to increase the capability to manipulate and record from the model
697 (e.g. spontaneous synaptic release, alter connectivity, extracellular LFP recording, and apply a variety
698 of stimuli). In short, the aim was to offer a more realistic yet scalable and sustainable approach to
699 model brain regions at full scale.

3.3 Future directions

701 There are some clear directions that would improve a full-scale atlas-based model of rat CA1. First,
702 large-scale models should include other feedforward synaptic pathways such as from CA2 (Tao et al.,
703 2021) and entorhinal cortex (EC) (Amaral & Witter, 1989), and back-propagating pathways such as from
704 subiculum (Jackson et al., 2014). Second, to date none of the large-scale models cover all the cell classes
705 found in the hippocampus (e.g. see Pelkey et al., 2017). For instance, interneuron-specific interneurons
706 (ISIs), estimated to represent about 20% of CA1 interneurons (see Bezaire and Soltesz, 2013), and their
707 disinhibitory influence have to date been absent in all large-scale circuit models. Third, improvements are
708 needed to represent *in vivo* conditions associated with different brain states more accurately to facilitate
709 easier comparisons with corresponding empirical data such as theta-phase preference of morphological
710 cell types (e.g. Klausberger et al., 2003). Fourth, while Yu et al. (2020) introduced topographic
711 connectivity for EC-DG-CA3 projections based on a 2D flat map, topographic projections such as from
712 CA3 to CA1 are best described in 3D space (e.g. Ishizuka et al., 1990) and they can be more accurately
713 represented in atlas-based circuits. Fifth, a variety of structural and functional gradients in hippocampus
714 have not been adequately modeled, e.g. differences in connectivity and responses along the dorsoventral
715 axis of CA1 (Lyttle et al., 2013; Malik et al., 2016a; Papatheodoropoulos, 2015), which may be important
716 in behavior. Again, atlas-based circuits are better suited for this task where dorsal and ventral regions
717 are predefined. Beyond this, other afferent inputs (e.g. perforant pathway) and circuit properties such
718 as gap junctions (e.g. Amsalem et al., 2016; Mercer, 2012; Mercer et al., 2006) and long-term synaptic
719 plasticity (e.g. Chindemi et al., 2022) could be incorporated.

720 In general, anchoring a circuit model in the volumetric space of a brain region atlas makes mapping
721 experimental data for data integration, validation and prediction easier than for more abstract spaces.
722 The Allen Brain Atlas has, for instance, demonstrated the advantages of registering community ex-
723 perimental data in a common reference atlas (Wang et al., 2020) and a common framework appears
724 advantageous for modeling as well. The piecemeal approach of constructing circuits for a specific use

725 case has short-term advantages for practicality but in the long run, a community reference circuit model,
726 that also has flexibility for customization and embodies reproducibility, makes comparing results easier
727 and offers a longer-term gain for investing in the modeling of any brain region.

3.4 Lessons learned

729 In the context of a community effort, the process of curating and integrating available data to reconstruct
730 a brain region and replicating the experimental conditions *in silico* proved instructive in a number of
731 ways.

732 Assembling the components to reconstruct a brain region naturally reveals gaps in the available data and
733 knowledge. Notably, for instance, while Schaffer collateral input to CA1 has received many decades of
734 attention, especially in terms of long-term plasticity, we found the basic information needed to model this
735 pathway quantitatively, was limited. To address this gap, we devised a multi-step algorithm constrained
736 by the data that were available to parametrize these connections. The process of assembling the
737 components can also reveal whether our inferences and assumptions are weak or can hold. For example,
738 we initially assumed that connectivity algorithm parameters derived for cortex (Markram et al., 2015)
739 could be re-used in hippocampus. However, this overestimated E→E and underestimated E→I synaptic
740 connections. We revised our assumption for these parameter values.

741 While an open source rat hippocampal atlas (Ropireddy et al., 2012) was crucial to reconstruct CA1, the
742 original volumetric reconstruction was too noisy for our purposes and required additional processing to
743 give smooth layering. This smoothness was necessary to place and orient morphologies accurately in the
744 atlas in relation to the layers. If the morphology was incorrectly placed or oriented, this had a knock-on
745 effect for how the circuit was connected. Similarly, the completeness of morphological reconstructions
746 also affected connectivity. For these reasons, some cell types in our available dataset could not be used
747 in the circuit model, sacrificing a small amount of cell type diversity in favor of completeness.

748 Setting up simulations to reproduce the desired experimental conditions requires careful attention. We
749 offer two examples from our research. First, when reproducing the I-O gain of SC afferent input
750 reported in Sasaki et al. (2006), we initially sampled all neurons in the model slice to plot to the I-O
751 curve. However, the result was poor. We later resolved this by following their experimental sampling of
752 a subset of neurons with which we could closely match the empirical curve. Second, when reproducing
753 MS-induced theta oscillations, we initially simulated under default conditions of extracellular calcium
754 concentration at 2 mM, resulting in theta oscillations that occurred episodically and only for a restricted
755 parameter regime. However, when we lowered the extracellular calcium to *in vivo* levels (1 mM), sparser
756 activity led to more robust and stable theta oscillations.

757 Computational methods and simulations allow the integration of sparse experimental results and provide
758 a framework to interpret them. For instance, the effects of ACh release on network activity have not been
759 fully elucidated yet, and it is not clear whether cholinergic agonism evokes oscillations in the CA1 region
760 (Bianchi & Wong, 1994; Fellous & Sejnowski, 2000; Fisahn et al., 1998; Pietersen et al., 2014; J. H.
761 Williams & Kauer, 1997). Our model predicts that a progressive increase in ACh concentration induces
762 a shift in network activity, which becomes initially highly correlated and then highly desynchronized at

high concentrations. Moreover, various mechanisms have been proposed for the generation of theta oscillations in CA1 (Colgin, 2013). Using our general model, while multiple mechanisms can potentially trigger theta oscillations in CA1, we observed that the neuronal dynamics induced by different extrinsic pacemakers were distinct. Only the medial septal disinhibition of PV+ interneurons was able to induce a theta rhythm compatible with observed *in vivo* firing phases of interneurons.

3.5 A community-driven modeling approach

The model was built and simulations run through the cooperation of several laboratories each with different expertise. Since we could not access a standardized core set of data made for the purpose of modeling as done previously (Iavarone et al., 2023; Markram et al., 2015; Reimann et al., 2022), instead, data had to be curated and integrated from different sources from labs following different protocols. The majority of single neuron morphologies and recordings, for instance, came from University College London (UCL) (Ali et al., 1998; Ali & Thomson, 2008; Ali et al., 1999; Fuentealba et al., 2008; Hughes et al., 2000; Mercer et al., 2006; Pawelzik et al., 1999, 2002; Thomson et al., 2000). From these data, single neuron models were created between the Blue Brain Project (BBP) and Italian National Research Council (CNR) (R. Migliore et al., 2018) and these were then validated by a computational lab at Institute of Experimental Medicine, Budapest (KOKI) (Sáray et al., 2021). Similarly, physiological data from paired recordings that characterized individual synaptic pathways were provided by an experimental lab in KOKI and then curated and integrated together with BBP (Ecker et al., 2020). Subsequently, BBP used these single neuron and synapse models to build and share the circuit model so computational labs at BBP, CNR, and KOKI could simulate various hippocampal use cases, only some of which have been presented here. Combining the framework of Markram et al. (2015) with community data and collaboration resulted in the generalization and improvement of data curation and integration methods for more varied data, improvements in tools like BluePyOpt for optimizing neurons, and the development of a new tools such as HippoUnit to systematically validate and compare different single neuron models.

This approach offers important features that make an attractive case for adoption by the wider hippocampus community. The model components, validations, and circuit are openly available through a dedicated portal hippocampushub.eu to maximize transparency and to allow the community to examine and judge how the circuit model was built, validated, simulated and analyzed. This includes providing metadata and provenance to improve reproducibility. Consequently, the framework and tools are well positioned to incorporate new data from the wider community to help improve the model in an open, transparent and reproducible way. Finally, this circuit model can be extended to incorporate glia and vascular systems within the same framework (Zisis et al., 2021). These systems are fundamental to regulating neuronal activity and communication in health and disease (Giaume et al., 2010) and could be adapted to make atlas-based circuit models much more realistic embodiment of brain regions. To conclude, this breakthrough, community-driven approach has potential to enhance understanding of hippocampal function and contribute significantly to advancing neuroscience research.

4 Methods

4.1 Reconstruction

We followed and adapted the method described in Markram et al. (2015) and Reimann et al. (2022) to reconstruct a full-scale model of the rat hippocampus CA1 (Figure 1). In brief, we collected 3D morphological reconstructions, belonging to different morphological types. Initial reconstructions were curated to produce a library of morphologies. The library was mixed and matched with the initial set of single-cell models (Ecker et al., 2020; R. Migliore et al., 2018) to produce a library of Hodgkin-Huxley multicompartimental neuron models. We placed neuron models into the CA1 region volume (Ropireddy et al., 2012) according to available data on cell densities and composition. We derived the intrinsic connectivity following the method of Reimann et al. (2015), and assigned synaptic parameters as described in Ecker et al. (2020).

4.2 Schaffer collaterals

Schaffer collaterals were generated according to anatomical information and then functionalized leveraging previous work (Ecker et al., 2020; Markram et al., 2015). The number of fibers was constrained considering the ratio between CA3 PCs and CA1 PCs and then connected with target in-degree ratios on CA1 PCs and INTs. Finally, synaptic physiology parameters were drawn from distributions with means and standard deviations specifically optimized for SC→PC and SC→INT projections.

4.3 Cholinergic modulation

To model the effect of ACh release, we expand the initial work of Ramaswamy et al. (2018). We collected data on the effect of ACh on neurons and synapses. In the case of neurons, we sampled 100 instances for each m-type and computed how an amount of somatic current deflects the voltage (sub-threshold) or increases the firing rate (supra-threshold). We then modeled the effect of ACh concentration on somatic voltage and firing rate with a current that produced the same effect. For synapses, we sampled 1,000 random connections, and computed how a change in the parameter U_{SE} led to a change in somatic PSP. Next we incorporated the data on the effect of ACh concentration on PSP with a change in U_{SE}.

4.4 Model availability

The circuit and simulation output are in SONATA format (Dai et al., 2020). The entire model, its components, and the source data can be explored and downloaded from hippocampushub.eu.

4.5 Simulation

Unless it is otherwise specified, we ran simulations with the following default parameters: extracellular calcium concentration of 2 mM, extracellular magnesium concentration of 1 mM, acetylcholine concentration of $0\,\mu m$, spontaneous synaptic events (minis) absent, Schaffer collaterals disconnected, temperature of 34.0°C, action potential detected at axon initial segment (AIS), voltage initiated at -65 mV, time step of 0.025 ms, CoreNEURON as simulator. Default simulations were run over cylindrical microcircuits and stored the spike times of each neuron and somatic voltages with a time step of 0.025 ms. Analyses of the simulations normally excluded the first 1000 ms to remove an initial circuit transient.

4.6   Local field potential

The extracellular field potential in the simulations was estimated using EMSim (see Table 1) (Newton et al., 2021; Reimann et al., 2013). The transmembrane currents from all the neuronal compartments, necessary to estimate the extracellular signal, were acquired with a temporal resolution of 0.5 ms. The local field potential (LFP) signal was generated by the low-pass filtering of this extracellular field potential (< 400 Hz cutoff) and its spectral characteristics were then analyzed using the Elephant package (Denker et al., 2018). For more details, see supplementary section S1.22.1.

4.7   Statistical analysis

Unless otherwise stated, values are expressed as mean $\pm$ standard deviation. We generally perform correlation tests to compare model and experiment data, and results are reported as (Pearson correlation coefficient, p-value). When correlation test is not applicable, depending on the data availability, we perform a z-test, t-test or even a qualitative comparison between model and experimental data (see S1.24).

4.8   Visualization

Hippocampus circuit and simulations were visualized with Brayns software, while morphologies were visualized with NeuroMorphoVis (Abdellah et al., 2018) (see Table 1).

4.9   Available hardware

Simulations were run initially using Blue Brain IV (BB4) system and later Blue Brain 5 (BB5) system, hosted at the Swiss National Computing Center (CSCS) in Lugano, Switzerland. BB4 was based on IBM BlueGene/Q (Haring 2012) with 4,096 nodes consisting of 65,536 PowerPC A2 cores. BB5 is an HPE SGI 8600 (Hewlett Packard Enterprise 2019) platform with 200 Intel Skylake with 7,200 cores and later 880 Intel Cascade Lake nodes with 35,200 cores.

In Table S24, we list HPC resources required to run and analyze exemplar simulations in this paper. We note the major bottlenecks in simulating the circuit with individual columns such as the circuit size, presence of SC, type of recording (intracellular or LFP) and report on the amount of memory required to load and simulate the circuit as well as how much time it takes to run them. We observed that the amount of required resources varied between 3.7 GB - 1.56 TB (422x) depending on these parameters and the computation time diverged around 4.08x between NEURON and CoreNEURON simulators (Kumbhar et al., 2019).

4.10   Supplementary information

Supplemental information includes Supplemental methods, figures, and tables.

5   Funding

Institutes of Technology.

6 Acknowledgments

6.1 Author contributions

H.M. conceived and led the study. S.K., M.M., A.T., F.S., E.M., and A.M. co-led the study. A.M.T. and A.M. planned, performed and supervised electrophysiological experiments and neuron reconstructions. J.F. and S.L. performed reconstructions. A.R., J.B., A.A., D.B., K.K. planned and supervised on data integration, strategies and algorithms, model building, simulation experiments, and analysis. A.A., J.B., D.B., A.R. reconstructed Schaffer collaterals. A.A., C.C., J.B., A.R. modeled Acetylcholine. J.B. and A.R. worked on theta. A.A., J.B. and A.R. worked on oscillation propagation. F.S. and J-D.C. planned and supervised the development of algorithms, software and workflows, computing infrastructure, and technical integration. A.R., J.B., A.A., D.B., C.C., K.K. wrote the manuscript. A detailed listing of author contributions is available in the Supplemental materials.

6.2 Acknowledgments

The authors would like to thank all the people involved in the rat CA1 hippocampus project over the last years, in particular Attila Gulyás, Luc Guyot, and Arseny Povolotsky. We would also like to thank those who offered valuable advice or data: Giorgio Ascoli, Norbert Hájos, Jesse Jackson, Corette Wierenga, Sylvain Williams. Experimentalists who generated data for this project or who recorded, dye-filled and/or reconstructed neurons: A.B. Ali, A.P Bannister, R. Begum, N. Botcher, J. Deuchars, K. Eastlake, D. I. Hughes, M. Ilia, J. Kerkhoff, S. Kirchhecker, H. Pawelzik, and H. Trigg. D.C. West designed data collection and analysis software. We thank those who worked on the Explore feature of the Hippocampus hub: Anil Tuncel, Pavlo Getta, Caitlin Monney, Stefano Antonel, Alexander Dietz, and Liviu Soltuzu. Finally, we are indebted to Karin Holm for copy editing and publication advice and support.

7 Software used

Table 1 gives a list of software used in the paper.

Software Name	Source	Identifier
bbp-workflow	BBP/EPFL software package	not yet open source
BluePy	BBP/EPFL software package	not yet open source
BluePyEfe	BBP/EPFL software package	https://github.com/BlueBrain/BluePyEfe
BluePyOpt	BBP/EPFL software package	https://github.com/BlueBrain/BluePyOpt
BluePyMM	BBP/EPFL software package	https://github.com/BlueBrain/BluePyMM
Brainbuilder	BBP/EPFL software package	not yet open source
Brayns	BBP/EPFL software package	https://github.com/BlueBrain/Brayns
circuit-build	BBP/EPFL software package	not yet open source
CoreNEURON	BBP/EPFL software package	https://github.com/BlueBrain/CoreNeuron
eFEL	BBP/EPFL software package	https://github.com/BlueBrain/eFEL
Elephant	Elephant authors and contributors	https://doi.org/10.5281/zenodo.1186602
EMSim	BBP/EPFL software package	https://github.com/BlueBrain/EMSim
Hippounit	KOKI software package	https://github.com/KaliLab/hippounit
ITK-SNAP	University of Pennsylvania	http://www.itksnap.org/
morphology-workflows	BBP/EPFL software package	https://github.com/BlueBrain/morphology-workflows
mtspec	pypi python package	https://pypi.org/project/mtspec/
neo	The NeuralEnsemble Initiative	https://github.com/NeuralEnsemble/python-neo
NeuroMorphoVis	BBP/EPFL software package	https://github.com/BlueBrain/NeuroMorphoVis
NeuroM	BBP/EPFL software package	https://github.com/BlueBrain/NeuroM
NeuroR	BBP/EPFL software package	https://github.com/BlueBrain/NeuroR
projectionizer	BBP/EPFL software package	not yet open source
psp-validation	BBP/EPFL software package	not yet open source
regiodesics	BBP/EPFL software package	not yet open source
TMD	BBP/EPFL software package	https://github.com/BlueBrain/TMD
voxcell	BBP/EPFL software package	https://github.com/BlueBrain/voxcell

Table 1: List of software used

8 References

Aad, G., & Abbott, B. (2015). Combined measurement of the Higgs boson mass in pp collisions at $\sqrt{s} = 7$ and 8 TeV with the ATLAS and CMS experiments. *Physical Review Letters*, *114*(19). https://doi.org/10.1103/physrevlett.114.191803

Abdellah, M., Hernando, J., Eilemann, S., Lapere, S., Antille, N., Markram, H., & Schürmann, F. (2018). NeuroMorphoVis: A collaborative framework for analysis and visualization of neuronal morphology skeletons reconstructed from microscopy stacks. *Bioinformatics (Oxford, England)*, *34*(13), i574–i582. https://doi.org/10.1093/bioinformatics/bty231

Addison, P., Walker, J., & Guido, R. (2009). Time–frequency analysis of biosignals. *IEEE Eng. Med. Biol. Mag.*, *28*(5), 14–29. https://doi.org/10.1109/MEMB.2009.934244

Agoston, M. K. (2004). *Computer graphics and geometric modeling: Implementation and algorithms*. Springer.

Aika, Y., Ren, J., Kosaka, K., & Kosaka, T. (1994). Quantitative analysis of GABA-like-immunoreactive and parvalbumin-containing neurons in the CA1 region of the rat hippocampus using a stereological method, the disector. *Experimental Brain Research*, *99*(2). https://doi.org/10.1007/BF00239593

Ali, A. B., Deuchars, J., Pawelzik, H., & Thomson, A. M. (1998). CA1 pyramidal to basket and bistratified cell EPSPs: Dual intracellular recordings in rat hippocampal slices. *J. Physiol.*, *507 (Pt 1)*, 201–217.

Ali, A. B. (2011). CB1 modulation of temporally distinct synaptic facilitation among local circuit interneurons mediated by n-type calcium channels in CA1. *Journal of Neurophysiology*, *105*(3), 1051–1062. https://doi.org/10.1152/jn.00831.2010

Ali, A. B., Bannister, A. P., & Thomson, A. M. (1999). IPSPs elicited in CA1 pyramidal cells by putative basket cells in slices of adult rat hippocampus: Basket cell IPSPs in CA1 pyramidal cells. *European Journal of Neuroscience*, *11*(5), 1741–1753. https://doi.org/10.1046/j.1460-9568.1999.00592.x

Ali, A. B., & Thomson, A. M. (2008). Synaptic alpha 5 subunit-containing GABAA receptors mediate IPSPs elicited by dendrite-preferring cells in rat neocortex. *Cereb. Cortex*, *18*(6), 1260–1271.

Amaral, D. G., & Witter, M. P. (1989). The three-dimensional organization of the hippocampal formation: A review of anatomical data. *Neuroscience*, *31*(3), 571–591. https://doi.org/10.1016/0306-4522(89)90424-7

Amsalem, O., Van Geit, W., Muller, E., Markram, H., & Segev, I. (2016). From neuron biophysics to orientation selectivity in electrically coupled networks of neocortical l2/3 large basket cells. *Cereb. Cortex*, *26*(8), 3655–3668. https://doi.org/10.1093/cercor/bhw166

Andrásfalvy, B. K., & Magee, J. C. (2001). Distance-dependent increase in AMPA receptor number in the dendrites of adult hippocampal CA1 pyramidal neurons. *The Journal of Neuroscience*, *21*(23), 9151–9159. https://doi.org/10.1523/JNEUROSCI.21-23-09151.2001

Anwar, H., Riachi, I., Hill, S., Schürmann, F., & Markram, H. (2009). An approach to capturing neuron morphological diversity. In *Computational modeling methods for neuroscientists* (pp. 211–232). The MIT Press. https://doi.org/10.7551/mitpress/9780262013277.003.0010

Ascoli, G. A., Gasparini, S., Medinilla, V., & Migliore, M. (2010). Local control of postinhibitory rebound spiking in CA1 pyramidal neuron dendrites. *The Journal of Neuroscience: The Official Journal of*

the Society for Neuroscience, 30(18), 6434–6442. https://doi.org/10.1523/JNEUROSCI.4066-09.2010

Awile, O., Kumbhar, P., Cornu, N., Dura-Bernal, S., King, J. G., Lupton, O., Magkanaris, I., McDougal, R. A., Newton, A. J. H., Pereira, F., Savulescu, A., Carnevale, N. T., Lytton, W. W., Hines, M. L., & Schurmann, F. (2022). Modernizing the NEURON simulator for sustainability, portability, and performance. Front. Neuroinform., 16, 884046. https://doi.org/10.3389/fninf.2022.884046

Baimbridge, K. G., & Miller, J. J. (1982). Immunohistochemical localization of calcium-binding protein in the cerebellum, hippocampal formation and olfactory bulb of the rat. Brain Research, 245(2), 223–229. https://doi.org/10.1016/0006-8993(82)90804-6

Bannister, N. J., & Larkman, A. U. (1995). Dendritic morphology of CA1 pyramidal neurones from the rat hippocampus: I. branching patterns. The Journal of Comparative Neurology, 360(1), 150–160. https://doi.org/10.1002/cne.903600111

Barros-Zulaica, N., Rahmon, J., Chindemi, G., Perin, R., Markram, H., Muller, E., & Ramaswamy, S. (2019). Estimating the readily-releasable vesicle pool size at synaptic connections in the neocortex. Frontiers in Synaptic Neuroscience, 11, 29. https://doi.org/10.3389/fnsyn.2019.00029

Belluscio, M. A., Mizuseki, K., Schmidt, R., Kempter, R., & Buzsáki, G. (2012). Cross-frequency phase-phase coupling between theta and gamma oscillations in the hippocampus. J. Neurosci., 32(2), 423–435. https://doi.org/10.1523/JNEUROSCI.4122-11.2012

Bezaire, M. J., Raikov, I., Burk, K., Vyas, D., & Soltesz, I. (2016). Interneuronal mechanisms of hippocampal theta oscillations in a full-scale model of the rodent CA1 circuit. eLife, 5. https://doi.org/10.7554/eLife.18566

Bezaire, M. J., & Soltesz, I. (2013). Quantitative assessment of CA1 local circuits: Knowledge base for interneuron-pyramidal cell connectivity: Quantitative assessment of ca1 local circuits. Hippocampus, 23(9), 751–785. https://doi.org/10.1002/hipo.22141

Bianchi, R., & Wong, R. K. (1994). Carbachol-induced synchronized rhythmic bursts in CA3 neurons of guinea pig hippocampus in vitro. Journal of Neurophysiology, 72(1), 131–138. https://doi.org/10.1152/jn.1994.72.1.131

Biro, A. A. (2005). Quantal size is independent of the release probability at hippocampal excitatory synapses. Journal of Neuroscience, 25(1), 223–232. https://doi.org/10.1523/JNEUROSCI.3688-04.2005

Bokil, H., Andrews, P., Kulkarni, J. E., Mehta, S., & Mitra, P. P. (2010). Chronux: A platform for analyzing neural signals. J. Neurosci. Methods, 192(1), 146–151. https://doi.org/10.1016/j.jneumeth.2010.06.020

Brankack, J., Stewart, M., & Fox, S. E. (1993). Current source density analysis of the hippocampal theta rhythm: Associated sustained potentials and candidate synaptic generators. Brain Res., 615(2), 310–327. https://doi.org/10.1016/0006-8993(93)90043-m

Buchanan, K. A., Petrovic, M. M., Chamberlain, S. E., Marrion, N. V., & Mellor, J. R. (2010). Facilitation of long-term potentiation by muscarinic m1 receptors is mediated by inhibition of SK channels. Neuron, 68(5), 948–963. https://doi.org/10.1016/j.neuron.2010.11.018

Buhl, E. H., Han, Z. S., Lorinczi, Z., Stezhka, V. V., Karnup, S. V., & Somogyi, P. (1994). Physiological properties of anatomically identified axo-axonic cells in the rat hippocampus. *Journal of Neurophysiology*, *71*(4), 1289–1307. https://doi.org/10.1152/jn.1994.71.4.1289

Buhl, E. H., Halasy, K., & Somogyi, P. (1994). Diverse sources of hippocampal unitary inhibitory postsynaptic potentials and the number of synaptic release sites. *Nature*, *368*(6474), 823–828. https://doi.org/10.1038/368823a0

Buzsáki, G., Rappelsberger, P., & Kellényi, L. (1985). Depth profiles of hippocampal rhythmic slow activity ('theta rhythm') depend on behaviour. *Electroencephalogr. Clin. Neurophysiol.*, *61*(1), 77–88. https://doi.org/10.1016/0013-4694(85)91075-2

Buzsáki, G. (2002). Theta oscillations in the hippocampus. *Neuron*, *33*(3), 325–340. https://doi.org/10.1016/s0896-6273(02)00586-x

Buzsáki, G. (2005). Theta rhythm of navigation: Link between path integration and landmark navigation, episodic and semantic memory. *Hippocampus*, *15*(7), 827–840. https://doi.org/10.1002/hipo.20113

Buzsáki, G. (2015). Hippocampal sharp wave-ripple: A cognitive biomarker for episodic memory and planning: HIPPOCAMPAL SHARP WAVE-RIPPLE. *Hippocampus*, *25*(10), 1073–1188. https://doi.org/10.1002/hipo.22488

Cea-del Rio, C. A., Lawrence, J. J., Erdelyi, F., Szabó, G., & McBain, C. J. (2011). Cholinergic modulation amplifies the intrinsic oscillatory properties of CA1 hippocampal cholecystokinin-positive interneurons: Cholinergic modulation and CA1 cholecystokinin-positive interneurons. *The Journal of Physiology*, *589*(3), 609–627. https://doi.org/10.1113/jphysiol.2010.199422

Chindemi, G., Abdellah, M., Amsalem, O., Benavides-Piccione, R., Delattre, V., Doron, M., Ecker, A., Jaquier, A. T., King, J., Kumbhar, P., Monney, C., Perin, R., Rössert, C., Tuncel, A. M., Van Geit, W., DeFelipe, J., Graupner, M., Segev, I., Markram, H., & Muller, E. B. (2022). A calcium-based plasticity model for predicting long-term potentiation and depression in the neocortex. *Nat. Commun.*, *13*(1), 3038. https://doi.org/10.1038/s41467-022-30214-w

Colangelo, C., Shichkova, P., Keller, D., Markram, H., & Ramaswamy, S. (2019). Cellular, synaptic and network effects of acetylcholine in the neocortex. *Frontiers in Neural Circuits*, *13*, 24. https://doi.org/10.3389/fncir.2019.00024

Colgin, L. L. (2013). Mechanisms and functions of theta rhythms. *Annual Review of Neuroscience*, *36*, 295–312. https://doi.org/10.1146/annurev-neuro-062012-170330

Cornford, J. H., Mercier, M. S., Leite, M., Magloire, V., Häusser, M., & Kullmann, D. M. (2019). Dendritic NMDA receptors in parvalbumin neurons enable strong and stable neuronal assemblies (M. Bartos, G. L. Westbrook, C.-C. Lien, & J. C. Poncer, Eds.). *eLife*, *8*, e49872. https://doi.org/10.7554/eLife.49872

Cossart, R., Hirsch, J. C., Cannon, R. C., Dinoncourt, C., Wheal, H. V., Ben-Ari, Y., Esclapez, M., & Bernard, C. (2000). Distribution of spontaneous currents along the somato-dendritic axis of rat hippocampal CA1 pyramidal neurons. *Neuroscience*, *99*(4), 593–603. https://doi.org/10.1016/s0306-4522(00)00231-1

Csicsvari, J., Hirase, H., Czurko, A., & Buzsáki, G. (1998). Reliability and state dependence of pyramidal cell-interneuron synapses in the hippocampus: An ensemble approach in the behaving rat. *Neuron*, *21*(1), 179–189. https://doi.org/10.1016/s0896-6273(00)80525-5

1028 Csicsvari, J., Hirase, H., Czurkó, A., Mamiya, A., & Buzsáki, G. (1999). Oscillatory coupling of hip-
1029   pocampal pyramidal cells and interneurons in the behaving rat. *J. Neurosci.*, *19*(1), 274–287.
1030   https://doi.org/10.1523/JNEUROSCI.19-01-00274.1999

1031 Cutsuridis, V., Cobb, S., & Graham, B. P. (2010). Encoding and retrieval in a model of the hippocampal
1032   CA1 microcircuit. *Hippocampus*, *20*(3), 423–446. https://doi.org/10.1002/hipo.20661

1033 Dai, K., Hernando, J., Billeh, Y. N., Gratiy, S. L., Planas, J., Davison, A. P., Dura-Bernal, S., Gleeson,
1034   P., Devresse, A., Dichter, B. K., Gevaert, M., King, J. G., Van Geit, W. A. H., Povolotsky,
1035   A. V., Muller, E., Courcol, J.-D., & Arkhipov, A. (2020). The SONATA data format for efficient
1036   description of large-scale network models. *PLoS computational biology*, *16*(2), e1007696. https:
1037   //doi.org/10.1371/journal.pcbi.1007696

1038 Dannenberg, H., Young, K., & Hasselmo, M. (2017). Modulation of hippocampal circuits by muscarinic
1039   and nicotinic receptors. *Front. Neural Circuits*, *11*, 102. https://doi.org/10.3389/fncir.2017.
1040   00102

1041 Dasari, S., & Gulledge, A. T. (2011). M1 and m4 receptors modulate hippocampal pyramidal neurons.
1042   *Journal of Neurophysiology*, *105*(2), 779–792. https://doi.org/10.1152/jn.00686.2010

1043 Debanne, D., Guérineau, N. C., Gähwiler, B. H., & Thompson, S. M. (1995). Physiology and phar-
1044   macology of unitary synaptic connections between pairs of cells in areas CA3 and CA1 of rat
1045   hippocampal slice cultures. *J. Neurophysiol.*, *73*(3), 1282–1294. https://doi.org/10.1152/jn.
1046   1995.73.3.1282

1047 Deguchi, Y., Donato, F., Galimberti, I., Cabuy, E., & Caroni, P. (2011). Temporally matched subpopu-
1048   lations of selectively interconnected principal neurons in the hippocampus. *Nature Neuroscience*,
1049   *14*(4), 495–504. https://doi.org/10.1038/nn.2768

1050 Denker, M., Yegenoglu, A., & Grün, S. (2018). Collaborative HPC-enabled workflows on the HBP
1051   collaboratory using the elephant framework [Publisher: G-Node]. https://doi.org/10.12751/
1052   INCF.NI2018.0019

1053 Deuchars, J., & Thomson, A. (1996). CA1 pyramid-pyramid connections in rat hippocampus in vitro:
1054   Dual intracellular recordings with biocytin filling. *Neuroscience*, *74*(4), 1009–1018. https://doi.
1055   org/10.1016/0306-4522(96)00251-5

1056 Dumas, T. C., Uttaro, M. R., Barriga, C., Brinkley, T., Halavi, M., Wright, S. N., Ferrante, M., Evans,
1057   R. C., Hawes, S. L., & Sanders, E. M. (2018). Removal of area CA3 from hippocampal slices
1058   induces postsynaptic plasticity at schaffer collateral synapses that normalizes CA1 pyramidal cell
1059   discharge. *Neuroscience Letters*, *678*, 55–61. https://doi.org/10.1016/j.neulet.2018.05.011

1060 Ecker, A., Romani, A., Sáray, S., Káli, S., Migliore, M., Falck, J., Lange, S., Mercer, A., Thomson, A. M.,
1061   Muller, E., Reimann, M. W., & Ramaswamy, S. (2020). Data-driven integration of hippocampal
1062   CA1 synaptic physiology in silico. *Hippocampus*, *30*(11), 1129–1145. https://doi.org/10.1002/
1063   hipo.23220

1064 Economides, G., Falk, S., & Mercer, A. (2018). Biocytin recovery and 3D reconstructions of filled
1065   hippocampal CA2 interneurons. *J. Vis. Exp.*, (141). https://doi.org/10.3791/58592

1066 Elfant, D., Pál, B. Z., Emptage, N., & Capogna, M. (2008). Specific inhibitory synapses shift the balance
1067   from feedforward to feedback inhibition of hippocampal CA1 pyramidal cells. *The European
1068   Journal of Neuroscience*, *27*(1), 104–113. https://doi.org/10.1111/j.1460-9568.2007.06001.x

Esclapez, M., Hirsch, J. C., Ben-Ari, Y., & Bernard, C. (1999a). Newly formed excitatory pathways provide a substrate for hyperexcitability in experimental temporal lobe epilepsy. *J. Comp. Neurol.*, *408*(4), 449–460. https://doi.org/10.1002/(sici)1096-9861(19990614)408:4<449::aid-cne1>3.0.co;2-r

Esclapez, M., Hirsch, J. C., Ben-Ari, Y., & Bernard, C. (1999b). Newly formed excitatory pathways provide a substrate for hyperexcitability in experimental temporal lobe epilepsy. *The Journal of Comparative Neurology*, *408*(4), 449–460. https://doi.org/10.1002/(SICI)1096-9861(19990614)408:4<449::AID-CNE1>3.0.CO;2-R

Fan, X., & Markram, H. (2019). A brief history of simulation neuroscience. *Front. Neuroinform.*, *13*, 32. https://doi.org/10.3389/fninf.2019.00032

Fellous, J. M., & Sejnowski, T. J. (2000). Cholinergic induction of oscillations in the hippocampal slice in the slow (0.5-2 hz), theta (5-12 hz), and gamma (35-70 hz) bands. *Hippocampus*, *10*(2), 187–197. https://doi.org/10.1002/(SICI)1098-1063(2000)10:2<187::AID-HIPO8>3.0.CO;2-M

Fisahn, A., Pike, F. G., Buhl, E. H., & Paulsen, O. (1998). Cholinergic induction of network oscillations at 40 hz in the hippocampus in vitro. *Nature*, *394*(6689), 186–189. https://doi.org/10.1038/28179

Földy, C., Lee, S.-H., Morgan, R. J., & Soltesz, I. (2010). Regulation of fast-spiking basket cell synapses by the chloride channel ClC-2. *Nature Neuroscience*, *13*(9), 1047–1049. https://doi.org/10.1038/nn.2609

Freund, T., & Buzsáki, G. (1996). Interneurons of the hippocampus. *Hippocampus*, *6*(4), 347–470. https://doi.org/10.1002/(SICI)1098-1063(1996)6:4<347::AID-HIPO1>3.0.CO;2-I

Fuentealba, P., Begum, R., Capogna, M., Jinno, S., Márton, L. F., Csicsvari, J., Thomson, A., Somogyi, P., & Klausberger, T. (2008). Ivy cells: A population of nitric-oxide-producing, slow-spiking GABAergic neurons and their involvement in hippocampal network activity. *Neuron*, *57*(6), 917–929. https://doi.org/10.1016/j.neuron.2008.01.034

Fuhrmann, G., Segev, I., Markram, H., & Tsodyks, M. (2002). Coding of temporal information by activity-dependent synapses. *Journal of Neurophysiology*, *87*(1), 140–148. https://doi.org/10.1152/jn.00258.2001

Gal, E., London, M., Globerson, A., Ramaswamy, S., Reimann, M. W., Muller, E., Markram, H., & Segev, I. (2017). Rich cell-type-specific network topology in neocortical microcircuitry. *Nature Neuroscience*, *20*(7), 1004–1013. https://doi.org/10.1038/nn.4576

Gerkin, R. C., Jarvis, R. J., & Crook, S. M. (2018). Towards systematic, data-driven validation of a collaborative, multi-scale model of caenorhabditis elegans. *Philos. Trans. R. Soc. Lond. B Biol. Sci.*, *373*(1758). https://doi.org/10.1098/rstb.2017.0381

Giacopelli, G., Tegolo, D., Spera, E., & Migliore, M. (2021). On the structural connectivity of large-scale models of brain networks at cellular level. *Scientific Reports*, *11*(1), 4345. https://doi.org/10.1038/s41598-021-83759-z

Giaume, C., Koulakoff, A., Roux, L., Holcman, D., & Rouach, N. (2010). Astroglial networks: A step further in neuroglial and gliovascular interactions. *Nat. Rev. Neurosci.*, *11*(2), 87–99. https://doi.org/10.1038/nrn2757

Glickfeld, L. L., & Scanziani, M. (2006). Distinct timing in the activity of cannabinoid-sensitive and cannabinoid-insensitive basket cells. *Nature Neuroscience*, *9*(6), 807–815. https://doi.org/10.1038/nn1688

Golding, N. L., Kath, W. L., & Spruston, N. (2001). Dichotomy of action-potential backpropagation in CA1 pyramidal neuron dendrites. *J. Neurophysiol.*, *86*(6), 2998–3010. https://doi.org/10.1152/jn.2001.86.6.2998

Goutagny, R., Jackson, J., & Williams, S. (2009). Self-generated theta oscillations in the hippocampus. *Nature Neuroscience*, *12*(12), 1491–1493. https://doi.org/10.1038/nn.2440

Goyal, A., Miller, J., Qasim, S. E., Watrous, A. J., Zhang, H., Stein, J. M., Inman, C. S., Gross, R. E., Willie, J. T., Lega, B., Lin, J.-J., Sharan, A., Wu, C., Sperling, M. R., Sheth, S. A., McKhann, G. M., Smith, E. H., Schevon, C., & Jacobs, J. (2020). Functionally distinct high and low theta oscillations in the human hippocampus. *Nature Communications*, *11*(1), 2469. https://doi.org/10.1038/s41467-020-15670-6

Grastyan, E., Lissak, K., Madarasz, I., & Donhoffer, H. (1959). Hippocampal electrical activity during the development of conditioned reflexes. *Electroencephalogr. Clin. Neurophysiol.*, *11*(3), 409–430. https://doi.org/10.1016/0013-4694(59)90040-9

Graves, A. R., Moore, S. J., Bloss, E. B., Mensh, B. D., Kath, W. L., & Spruston, N. (2012). Hippocampal pyramidal neurons comprise two distinct cell types that are countermodulated by metabotropic receptors. *Neuron*, *76*(4), 776–789. https://doi.org/10.1016/j.neuron.2012.09.036

Green, J. D., & Arduini, A. A. (1954). Hippocampal electrical activity in arousal. *J. Neurophysiol.*, *17*(6), 533–557. https://doi.org/10.1152/jn.1954.17.6.533

Hájos, N., & Mody, I. (1997). Synaptic communication among hippocampal interneurons: Properties of spontaneous IPSCs in morphologically identified cells. *J. Neurosci.*, *17*(21), 8427–8442.

Hangya, B., Borhegyi, Z., Szilágyi, N., Freund, T. F., & Varga, V. (2009). GABAergic neurons of the medial septum lead the hippocampal network during theta activity. *The Journal of Neuroscience: The Official Journal of the Society for Neuroscience*, *29*(25), 8094–8102. https://doi.org/10.1523/JNEUROSCI.5665-08.2009

Hasselmo, M., & Schnell, E. (1994). Laminar selectivity of the cholinergic suppression of synaptic transmission in rat hippocampal region CA1: Computational modeling and brain slice physiology. *The Journal of Neuroscience*, *14*(6), 3898–3914. https://doi.org/10.1523/JNEUROSCI.14-06-03898.1994

Hasselmo, M. E. (2006). The role of acetylcholine in learning and memory. *Current Opinion in Neurobiology*, *16*(6), 710–715. https://doi.org/10.1016/j.conb.2006.09.002

Hasselmo, M. E., Alexander, A. S., Dannenberg, H., & Newman, E. L. (2020). Overview of computational models of hippocampus and related structures: Introduction to the special issue. *Hippocampus*, *30*(4), 295–301. https://doi.org/10.1002/hipo.23201

Hoffman, D. A., & Johnston, D. (1999). Neuromodulation of dendritic action potentials. *J. Neurophysiol.*, *81*(1), 408–411. https://doi.org/10.1152/jn.1999.81.1.408

Hoffman, D. A., Magee, J. C., Colbert, C. M., & Johnston, D. (1997). K+ channel regulation of signal propagation in dendrites of hippocampal pyramidal neurons. *Nature*, *387*(6636), 869–875. https://doi.org/10.1038/43119

Hood, L., & Rowen, L. (2013). The human genome project: Big science transforms biology and medicine. *Genome Medicine*, *5*(9), 79. https://doi.org/10.1186/gm483

Hu, H., Martina, M., & Jonas, P. (2010). Dendritic mechanisms underlying rapid synaptic activation of fast-spiking hippocampal interneurons. *Science (New York, N.Y.)*, *327*(5961), 52–58. https://doi.org/10.1126/science.1177876

Hughes, D. I., Bannister, A., Pawelzik, H., & Thomson, A. M. (2000). Double immunofluorescence, peroxidase labelling and ultrastructural analysis of interneurones following prolonged electro-physiological recordings in vitro. *Journal of Neuroscience Methods*, *101*(2), 107–116. https://doi.org/10.1016/S0165-0270(00)00254-5

Iavarone, E., Simko, J., Shi, Y., Bertschy, M., Garcıa-Amado, M., Litvak, P., Kaufmann, A.-K., O'Reilly, C., Amsalem, O., Abdellah, M., Chevtchenko, G., Coste, B., Courcol, J.-D., Ecker, A., Favreau, C., Fleury, A. C., Van Geit, W., Gevaert, M., Guerrero, N. R., . . . Hill, S. L. (2023). Thalamic control of sensory processing and spindles in a biophysical somatosensory thalamoreticular circuit model of wakefulness and sleep. *Cell Rep.*, *42*(3), 112200. https://doi.org/10.1016/j.celrep.2023.112200

Ishizuka, N., Weber, J., & Amaral, D. G. (1990). Organization of intrahippocampal projections originating from CA3 pyramidal cells in the rat. *J. Comp. Neurol.*, *295*(4), 580–623. https://doi.org/10.1002/cne.902950407

Ito, H. T., & Schuman, E. M. (2009). Distance-dependent homeostatic synaptic scaling mediated by a-type potassium channels. *Front. Cell. Neurosci.*, *3*, 15. https://doi.org/10.3389/neuro.03.015.2009

Jackson, J., Amilhon, B., Goutagny, R., Bott, J.-B., Manseau, F., Kortleven, C., Bressler, S. L., & Williams, S. (2014). Reversal of theta rhythm flow through intact hippocampal circuits. *Nature Neuroscience*, *17*(10), 1362–1370. https://doi.org/10.1038/nn.3803

Jung, R., & Kornmüller, A. E. (1938). Eine methodik der ableitung iokalisierter potentialschwankungen aus subcorticalen hirngebieten. *Archiv für Psychiatrie und Nervenkrankheiten*, *109*(1), 1–30. https://doi.org/10.1007/BF02157817

Kamondi, A., Acsády, L., Wang, X. J., & Buzsáki, G. (1998). Theta oscillations in somata and dendrites of hippocampal pyramidal cells in vivo: Activity-dependent phase-precession of action potentials. *Hippocampus*, *8*(3), 244–261. https://doi.org/10.1002/(SICI)1098-1063(1998)8:3<244::AID-HIPO7>3.0.CO;2-J

Kanari, L., Dictus, H., Chalimourda, A., Arnaudon, A., Van Geit, W., Coste, B., Shillcock, J., Hess, K., & Markram, H. (2022). Computational synthesis of cortical dendritic morphologies. *Cell Reports*, *39*(1), 110586. https://doi.org/10.1016/j.celrep.2022.110586

Kanari, L., Dłotko, P., Scolamiero, M., Levi, R., Shillcock, J., Hess, K., & Markram, H. (2018). A topological representation of branching neuronal morphologies. *Neuroinformatics*, *16*(1), 3–13. https://doi.org/10.1007/s12021-017-9341-1

Kawasaki, H., & Avoli, M. (1996). Excitatory effects induced by carbachol on bursting neurons of the rat subiculum. *Neuroscience Letters*, *219*(1), 1–4. https://doi.org/10.1016/S0304-3940(96)13175-X

Klausberger, T. (2005). Complementary roles of cholecystokinin- and parvalbumin-expressing GABAergic neurons in hippocampal network oscillations. *Journal of Neuroscience*, *25*(42), 9782–9793. https://doi.org/10.1523/JNEUROSCI.3269-05.2005

Klausberger, T., Magill, P. J., Márton, L. F., Roberts, J. D. B., Cobden, P. M., Buzsáki, G., & Somogyi, P. (2003). Brain-state- and cell-type-specific firing of hippocampal interneurons in vivo. *Nature*, *421*(6925), 844–848. https://doi.org/10.1038/nature01374

Klausberger, T., Márton, L. F., Baude, A., Roberts, J. D. B., Magill, P. J., & Somogyi, P. (2004). Spike timing of dendrite-targeting bistratified cells during hippocampal network oscillations in vivo. *Nature Neuroscience*, *7*(1), 41–47. https://doi.org/10.1038/nn1159

Knowles, W. D., & Schwartzkroin, P. A. (1981). Local circuit synaptic interactions in hippocampal brain slices [Publisher: Society for Neuroscience Section: Articles]. *Journal of Neuroscience*, *1*(3), 318–322. https://doi.org/10.1523/JNEUROSCI.01-03-00318.1981

Kocsis, B., Bragin, A., & Buzsáki, G. (1999). Interdependence of multiple theta generators in the hippocampus: A partial coherence analysis. *J. Neurosci.*, *19*(14), 6200–6212. https://doi.org/10.1523/JNEUROSCI.19-14-06200.1999

Kumbhar, P., Hines, M., Fouriaux, J., Ovcharenko, A., King, J., Delalondre, F., & Schürmann, F. (2019). Coreneuron : An optimized compute engine for the neuron simulator. *Frontiers in Neuroinformatics*, *13*. https://doi.org/10.3389/fninf.2019.00063

Lawrence, J. J., Statland, J. M., Grinspan, Z. M., & McBain, C. J. (2006). Cell type-specific dependence of muscarinic signalling in mouse hippocampal stratum oriens interneurones: mAChR modulation of str. oriens interneurones. *The Journal of Physiology*, *570*(3), 595–610. https://doi.org/10.1113/jphysiol.2005.100875

Le Bon-Jego, M., & Yuste, R. (2007). Persistently active, pacemaker-like neurons in neocortex. *Front. Neurosci.*, *1*(1), 123–129. https://doi.org/10.3389/neuro.01.1.1.009.2007

Le Roux, N., Cabezas, C., Böhm, U. L., & Poncer, J. C. (2013). Input-specific learning rules at excitatory synapses onto hippocampal parvalbumin-expressing interneurons. *The Journal of Physiology*, *591*(7), 1809–1822. https://doi.org/10.1113/jphysiol.2012.245852

Lee, S.-H., Marchionni, I., Bezaire, M., Varga, C., Danielson, N., Lovett-Barron, M., Losonczy, A., & Soltesz, I. (2014). Parvalbumin-positive basket cells differentiate among hippocampal pyramidal cells. *Neuron*, *82*(5), 1129–1144. https://doi.org/10.1016/j.neuron.2014.03.034

Lee, S.-H., Foldy, C., & Soltesz, I. (2010). Distinct endocannabinoid control of GABA release at perisomatic and dendritic synapses in the hippocampus. *Journal of Neuroscience*, *30*(23), 7993–8000. https://doi.org/10.1523/jneurosci.6238-09.2010

Li, X.-G., Somogyi, P., Ylinen, A., & Buzsáki, G. (1994). The hippocampal CA3 network: An in vivo intracellular labeling study: THE HIPPOCAMPAL CA3 NETWORK. *Journal of Comparative Neurology*, *339*(2), 181–208. https://doi.org/10.1002/cne.903390204

Lyttle, D., Gereke, B., Lin, K. K., & Fellous, J.-M. (2013). Spatial scale and place field stability in a grid-to-place cell model of the dorsoventral axis of the hippocampus. *Hippocampus*, *23*(8), 729–744. https://doi.org/10.1002/hipo.22132

Maccaferri, G., David, J., Roberts, B., Szucs, P., Cottingham, C. A., & Somogyi, P. (2000). Cell surface domain specific postsynaptic currents evoked by identified GABAergic neurones in rat hippocampus *in vitro*. *The Journal of Physiology*, *524*(1), 91–116. https://doi.org/10.1111/j.1469-7793.2000.t01-3-00091.x

Magee, J. C. (1999). Dendritic lh normalizes temporal summation in hippocampal CA1 neurons. *Nat. Neurosci.*, *2*(6), 508–514. https://doi.org/10.1038/9158

Magee, J. C., & Cook, E. P. (2000). Somatic EPSP amplitude is independent of synapse location in hippocampal pyramidal neurons. *Nat. Neurosci.*, *3*(9), 895–903. https://doi.org/10.1038/78800

Malik, R., Dougherty, K. A., Parikh, K., Byrne, C., & Johnston, D. (2016a). Mapping the electro-physiological and morphological properties of CA1 pyramidal neurons along the longitudinal hippocampal axis. *Hippocampus*, *26*(3), 341–361. https://doi.org/10.1002/hipo.22526

Malik, R., Dougherty, K. A., Parikh, K., Byrne, C., & Johnston, D. (2016b). Mapping the electro-physiological and morphological properties of CA1 pyramidal neurons along the longitudinal hippocampal axis. *Hippocampus*, *26*(3), 341–361. https://doi.org/10.1002/hipo.22526

Markram, H., Lübke, J., Frotscher, M., Roth, A., & Sakmann, B. (1997). Physiology and anatomy of synaptic connections between thick tufted pyramidal neurones in the developing rat neocortex. *The Journal of Physiology*, *500*, 409–440. Retrieved September 21, 2022, from https://www.ncbi.nlm.nih.gov/pmc/articles/PMC1159394/

Markram, H., Wang, Y., & Tsodyks, M. (1998). Differential signaling via the same axon of neocortical pyramidal neurons. *Proceedings of the National Academy of Sciences of the United States of America*, *95*(9), 5323–5328. https://doi.org/10.1073/pnas.95.9.5323

Markram, H., Muller, E., Ramaswamy, S., Reimann, M. W., Abdellah, M., Sanchez, C. A., Ailamaki, A., Alonso-Nanclares, L., Antille, N., Arsever, S., Kahou, G. A. A., Berger, T. K., Bilgili, A., Buncic, N., Chalimourda, A., Chindemi, G., Courcol, J.-D., Delalondre, F., Delattre, V., . . . Gidon, A. (2015). Reconstruction and simulation of neocortical microcircuitry. *Cell*, *163*(2), 456–492. https://doi.org/10.1016/j.cell.2015.09.029

McQuiston, A. R., & Madison, D. V. (1999). Muscarinic receptor activity has multiple effects on the resting membrane potentials of CA1 hippocampal interneurons. *The Journal of Neuroscience*, *19*(14), 5693–5702. https://doi.org/10.1523/JNEUROSCI.19-14-05693.1999

Megias, M., Emri, Z., Freund, T., & Gulyas, A. (2001). Total number and distribution of inhibitory and excitatory synapses on hippocampal CA1 pyramidal cells. *Neuroscience*, *102*(3), 527–540. https://doi.org/10.1016/S0306-4522(00)00496-6

Mercer, A. (2012). Electrically coupled excitatory neurones in cortical regions. *Brain Res.*, *1487*, 192–197. https://doi.org/10.1016/j.brainres.2012.03.069

Mercer, A., Bannister, A. P., & Thomson, A. M. (2006). Electrical coupling between pyramidal cells in adult cortical regions. *Brain Cell Biol.*, *35*(1), 13–27. https://doi.org/10.1007/s11068-006-9005-9

Migliore, M., Hoffman, D. A., Magee, J. C., & Johnston, D. (1999). Role of an a-type k+ conductance in the back-propagation of action potentials in the dendrites of hippocampal pyramidal neurons. *Journal of Computational Neuroscience*, *7*(1), 5–15. https://doi.org/10.1023/a:1008906225285

Migliore, M., Ferrante, M., & Ascoli, G. A. (2005). Signal propagation in oblique dendrites of CA1 pyramidal cells. *J. Neurophysiol.*, *94*(6), 4145–4155. https://doi.org/10.1152/jn.00521.2005

Migliore, R., Lupascu, C. A., Bologna, L. L., Romani, A., Courcol, J.-D., Antonel, S., Van Geit, W. A. H., Thomson, A. M., Mercer, A., Lange, S., Falck, J., Rössert, C. A., Shi, Y., Hagens, O., Pezzoli, M., Freund, T. F., Kali, S., Muller, E. B., Schürmann, F., . . . Migliore, M. (2018). The physiological variability of channel density in hippocampal CA1 pyramidal cells and interneurons explored using a unified data-driven modeling workflow (W. W. Lytton, Ed.). *PLOS Computational Biology*, *14*(9), e1006423. https://doi.org/10.1371/journal.pcbi.1006423

Milstein, A. D., Bloss, E. B., Apostolides, P. F., Vaidya, S. P., Dilly, G. A., Zemelman, B. V., & Magee, J. C. (2015). Inhibitory gating of input comparison in the CA1 microcircuit. *Neuron*, *87*(6), 1274–1289. https://doi.org/10.1016/j.neuron.2015.08.025

Mizuseki, K., Diba, K., Pastalkova, E., & Buzsáki, G. (2011). Hippocampal CA1 pyramidal cells form functionally distinct sublayers. *Nature Neuroscience*, *14*(9), 1174–1181. https://doi.org/10.1038/nn.2894

Moradi, K., & Ascoli, G. A. (2020). A comprehensive knowledge base of synaptic electrophysiology in the rodent hippocampal formation. *Hippocampus*, *30*(4), 314–331. https://doi.org/10.1002/hipo.23148

Morris, R. G., Garrud, P., Rawlins, J. N., & O'Keefe, J. (1982). Place navigation impaired in rats with hippocampal lesions. *Nature*, *297*(5868), 681–683. https://doi.org/10.1038/297681a0

Morse, T. M., Carnevale, N. T., Mutalik, P. G., Migliore, M., & Shepherd, G. M. (2010). Abnormal excitability of oblique dendrites implicated in early alzheimer's: A computational study. *Frontiers in Neural Circuits*, *4*, 16. https://doi.org/10.3389/fncir.2010.00016

Müller, C., & Remy, S. (2018). Septo–hippocampal interaction. *Cell and Tissue Research*, *373*(3), 565–575. https://doi.org/10.1007/s00441-017-2745-2

Neu, A., Földy, C., & Soltesz, I. (2007). Postsynaptic origin of CB1-dependent tonic inhibition of GABA release at cholecystokinin-positive basket cell to pyramidal cell synapses in the CA1 region of the rat hippocampus. *The Journal of Physiology*, *578*, 233–247. https://doi.org/10.1113/jphysiol.2006.115691

Newton, T. H., Reimann, M. W., Abdellah, M., Chevtchenko, G., Muller, E. B., & Markram, H. (2021). In silico voltage-sensitive dye imaging reveals the emergent dynamics of cortical populations. *Nature Communications*, *12*(1), 3630. https://doi.org/10.1038/s41467-021-23901-7

O'Keefe, J., & Dostrovsky, J. (1971). The hippocampus as a spatial map. preliminary evidence from unit activity in the freely-moving rat. *Brain Res.*, *34*(1), 171–175. https://doi.org/10.1016/0006-8993(71)90358-1

Palacios, J., Lida Kanari, Zisis, E., MikeG, Benoit Coste, Asanin-Epfl, Vanherpe, L., Jdcourcol, Arnaudon, A., Berchet, A., Haleepfl, Getta, P., Povolotsky, A. V., A Sato, Alex4200, Bbpgithubaudit, Ficarelli, G., Amsalem, O., Stefanoantonel, & Tomdele. (2022). Bluebrain/neurom: V3.2.2. https://doi.org/10.5281/ZENODO.597333

Palacios-Filardo, J., Udakis, M., Brown, G. A., Tehan, B. G., Congreve, M. S., Nathan, P. J., Brown, A. J. H., & Mellor, J. R. (2021). Acetylcholine prioritises direct synaptic inputs from entorhinal cortex to CA1 by differential modulation of feedforward inhibitory circuits. *Nature Communications*, *12*(1), 5475. https://doi.org/10.1038/s41467-021-25280-5

Papatheodoropoulos, C. (2015). Striking differences in synaptic facilitation along the dorsoventral axis of the hippocampus. *Neuroscience*, *301*, 454–470. https://doi.org/10.1016/j.neuroscience.2015.06.029

Pawelzik, H., Bannister, A. P., Deuchars, J., Ilia, M., & Thomson, A. M. (1999). Modulation of bistratifed cell IPSPs and basket cell IPSPs by pentobarbitone sodium, diazepam and zn2+: Dual recordings in slices of adult rat hippocampus. *European Journal of Neuroscience*, 13.

Pawelzik, H., Hughes, D. I., & Thomson, A. M. (2002). Physiological and morphological diversity of immunocytochemically defined parvalbumin- and cholecystokinin-positive interneurones in CA1

of the adult rat hippocampus. *The Journal of Comparative Neurology*, *443*(4), 346–367. https://doi.org/10.1002/cne.10118

Pelkey, K. A., Chittajallu, R., Craig, M. T., Tricoire, L., Wester, J. C., & McBain, C. J. (2017). Hippocampal GABAergic inhibitory interneurons. *Physiol. Rev.*, *97*(4), 1619–1747. https://doi.org/10.1152/physrev.00007.2017

Petilla Interneuron Nomenclature Group, Ascoli, G. A., Alonso-Nanclares, L., Anderson, S. A., Barrionuevo, G., Benavides-Piccione, R., Burkhalter, A., Buzsáki, G., Cauli, B., Defelipe, J., Fairén, A., Feldmeyer, D., Fishell, G., Fregnac, Y., Freund, T. F., Gardner, D., Gardner, E. P., Goldberg, J. H., Helmstaedter, M., . . . Yuste, R. (2008). Petilla terminology: Nomenclature of features of GABAergic interneurons of the cerebral cortex. *Nat. Rev. Neurosci.*, *9*(7), 557–568. https://doi.org/10.1038/nrn2402

Pietersen, A. N. J., Ward, P. D., Hagger-Vaughan, N., Wiggins, J., Jefferys, J. G. R., & Vreugdenhil, M. (2014). Transition between fast and slow gamma modes in rat hippocampus area CA1 in vitro is modulated by slow CA3 gamma oscillations. *The Journal of Physiology*, *592*(4), 605–620. https://doi.org/10.1113/jphysiol.2013.263889

Potworowski, J., Jakuczun, W., Leski, S., & Wojcik, D. (2012). Kernel current source density method. *Neural Comput.*, *24*(2), 541–575. https://doi.org/10.1162/NECO_a_00236

Pouille, F., & Scanziani, M. (2001). Enforcement of temporal fidelity in pyramidal cells by somatic feed-forward inhibition. *Science (New York, N.Y.)*, *293*(5532), 1159–1163. https://doi.org/10.1126/science.1060342

Pouille, F., Marin-Burgin, A., Adesnik, H., Atallah, B. V., & Scanziani, M. (2009). Input normalization by global feedforward inhibition expands cortical dynamic range. *Nature Neuroscience*, *12*(12), 1577–1585. https://doi.org/10.1038/nn.2441

Prieto, G. A., Parker, R. L., & Vernon, F. L., III. (2009). A fortran 90 library for multitaper spectrum analysis. *Comput. Geosci.*, *35*(8), 1701–1710. https://doi.org/10.1016/j.cageo.2008.06.007

Ramaswamy, S., Colangelo, C., & Markram, H. (2018). Data-driven modeling of cholinergic modulation of neural microcircuits: Bridging neurons, synapses and network activity. *Frontiers in Neural Circuits*, *12*, 77. https://doi.org/10.3389/fncir.2018.00077

Reimann, M. W., Anastassiou, C. A., Perin, R., Hill, S. L., Markram, H., & Koch, C. (2013). A biophysically detailed model of neocortical local field potentials predicts the critical role of active membrane currents. *Neuron*, *79*(2), 375–390. https://doi.org/10.1016/j.neuron.2013.05.023

Reimann, M. W., Bolaños-Puchet, S., Courcol, J.-D., Santander, D. E., Arnaudon, A., Coste, B., Delemontex, T., Devresse, A., Dictus, H., Dietz, A., Ecker, A., Favreau, C., Ficarelli, G., Gevaert, M., Hernando, J. B., Herttuainen, J., Isbister, J. B., Kanari, L., Keller, D., . . . Markram, H. (2022). Modeling and Simulation of Rat Non-Barrel Somatosensory Cortex. Part I: Modeling Anatomy. *bioRxiv*, 2022.08.11.503144. https://doi.org/10.1101/2022.08.11.503144

Reimann, M. W., King, J. G., Muller, E. B., Ramaswamy, S., & Markram, H. (2015). An algorithm to predict the connectome of neural microcircuits. *Frontiers in Computational Neuroscience*, *9*. https://doi.org/10.3389/fncom.2015.00120

Rockström, J., Steffen, W., Noone, K., Persson, Å., Chapin, F. S., Lambin, E. F., Lenton, T. M., Scheffer, M., Folke, C., Schellnhuber, H. J., Nykvist, B., de Wit, C. A., Hughes, T., van der Leeuw, S.,

Rodhe, H., Sörlin, S., Snyder, P. K., Costanza, R., Svedin, U., . . . Foley, J. A. (2009). A safe operating space for humanity. *Nature*, *461*(7263), 472–475. https://doi.org/10.1038/461472a

Romani, A., Schürmann, F., Markram, H., & Migliore, M. (2022). Reconstruction of the hippocampus. *Advances in Experimental Medicine and Biology*, *1359*, 261–283. https://doi.org/10.1007/978-3-030-89439-9_11

Ropireddy, D., Bachus, S., & Ascoli, G. (2012). Non-homogeneous stereological properties of the rat hippocampus from high-resolution 3d serial reconstruction of thin histological sections. *Neuroscience*, *205*, 91–111. https://doi.org/10.1016/j.neuroscience.2011.12.055

Sanchez-Aguilera, A., Wheeler, D. W., Jurado-Parras, T., Valero, M., Nokia, M. S., Cid, E., Fernandez-Lamo, I., Sutton, N., Garcia-Rincon, D., de la Prida, L. M., & Ascoli, G. A. (2021). An update to hippocampome.org by integrating single-cell phenotypes with circuit function in vivo. *PLoS biology*, *19*(5), e3001213. https://doi.org/10.1371/journal.pbio.3001213

Sáray, S., Rössert, C. A., Appukuttan, S., Migliore, R., Vitale, P., Lupascu, C. A., Bologna, L. L., Van Geit, W., Romani, A., Davison, A. P., Muller, E., Freund, T. F., & Káli, S. (2021). HippoUnit: A software tool for the automated testing and systematic comparison of detailed models of hippocampal neurons based on electrophysiological data. *PLoS Comput. Biol.*, *17*(1), e1008114. https://doi.org/10.1371/journal.pcbi.1008114

Sasaki, T., Kimura, R., Tsukamoto, M., Matsuki, N., & Ikegaya, Y. (2006). Integrative spike dynamics of rat CA1 neurons: A multineuronal imaging study. *The Journal of Physiology*, *574*, 195–208. https://doi.org/10.1113/jphysiol.2006.108480

Sayer, R. J., Friedlander, M. J., & Redman, S. J. (1990). The time course and amplitude of EPSPs evoked at synapses between pairs of CA3/CA1 neurons in the hippocampal slice. *The Journal of Neuroscience: The Official Journal of the Society for Neuroscience*, *10*(3), 826–836.

Sevilla, D. F., Cabezas, C., Prada, A. N. O., Sánchez-Jiménez, A., & Buño, W. (2002). Selective muscarinic regulation of functional glutamatergic schaffer collateral synapses in rat CA1 pyramidal neurons. *The Journal of Physiology*, *545*(1), 51–63. https://doi.org/10.1113/jphysiol.2002.029165

Shah, M. M., Migliore, M., Valencia, I., Cooper, E. C., & Brown, D. A. (2008). Functional significance of axonal kv7 channels in hippocampal pyramidal neurons. *Proc. Natl. Acad. Sci. U. S. A.*, *105*(22), 7869–7874. https://doi.org/10.1073/pnas.0802805105

Sheridan, R. D., & Sutor, B. (1990). Presynaptic m1 muscarinic cholinoceptors mediate inhibition of excitatory synaptic transmission in the hippocampus in vitro. *Neuroscience Letters*, *108*(3), 273–278. https://doi.org/10.1016/0304-3940(90)90653-Q

Siapas, A. G., Lubenov, E. V., & Wilson, M. A. (2005). Prefrontal phase locking to hippocampal theta oscillations. *Neuron*, *46*(1), 141–151. https://doi.org/10.1016/j.neuron.2005.02.028

Sik, A., Penttonen, M., Ylinen, A., & Buzsáki, G. (1995). Hippocampal CA1 interneurons: An in vivo intracellular labeling study. *The Journal of Neuroscience*, *15*(10), 6651–6665. https://doi.org/10.1523/JNEUROSCI.15-10-06651.1995

Sik, A., Tamamaki, N., & Freund, T. F. (1993). Complete axon arborization of a single CA3 pyramidal cell in the rat hippocampus, and its relationship with postsynaptic parvalbumin-containing interneurons. *European Journal of Neuroscience*, *5*(12), 1719–1728. https://doi.org/10.1111/j.1460-9568.1993.tb00239.x

Sirota, A., Montgomery, S., Fujisawa, S., Isomura, Y., Zugaro, M., & Buzsáki, G. (2008). Entrainment of neocortical neurons and gamma oscillations by the hippocampal theta rhythm. *Neuron*, *60*(4), 683–697. https://doi.org/10.1016/j.neuron.2008.09.014

Slomianka, L., Amrein, I., Knuesel, I., Sørensen, J. C., & Wolfer, D. P. (2011). Hippocampal pyramidal cells: The reemergence of cortical lamination. *Brain Structure & Function*, *216*(4), 301–317. https://doi.org/10.1007/s00429-011-0322-0

Sniedovich, M. (2006). Dijkstra's algorithm revisited: The dynamic programming connexion. *Control and Cybernetics*, 599–620. Retrieved August 2, 2022, from https://www.infona.pl//resource/bwmeta1.element.baztech-article-BAT5-0013-0005

Soltesz, I., & Losonczy, A. (2018). CA1 pyramidal cell diversity enabling parallel information processing in the hippocampus [Number: 4 Publisher: Nature Publishing Group]. *Nature Neuroscience*, *21*(4), 484–493. https://doi.org/10.1038/s41593-018-0118-0

Sun, Y., Nguyen, A. Q., Nguyen, J. P., Le, L., Saur, D., Choi, J., Callaway, E. M., & Xu, X. (2014). Cell-type-specific circuit connectivity of hippocampal CA1 revealed through cre-dependent rabies tracing. *Cell Reports*, *7*(1), 269–280. https://doi.org/10.1016/j.celrep.2014.02.030

Sutton, N. M., & Ascoli, G. A. (2021). Spiking neural networks and hippocampal function: A web-accessible survey of simulations, modeling methods, and underlying theories. *Cognitive Systems Research*, *70*, 80–92. https://doi.org/10.1016/j.cogsys.2021.07.008

Szabó, G. G., Holderith, N., Gulyás, A. I., Freund, T. F., & Hájos, N. (2010). Distinct synaptic properties of perisomatic inhibitory cell types and their different modulation by cholinergic receptor activation in the CA3 region of the mouse hippocampus: Synaptic properties of perisomatic interneurons. *European Journal of Neuroscience*, *31*(12), 2234–2246. https://doi.org/10.1111/j.1460-9568.2010.07292.x

Szigeti, B., Gleeson, P., Vella, M., Khayrulin, S., Palyanov, A., Hokanson, J., Currie, M., Cantarelli, M., Idili, G., & Larson, S. (2014). OpenWorm: An open-science approach to modeling caenorhabditis elegans. *Front. Comput. Neurosci.*, *8*, 137. https://doi.org/10.3389/fncom.2014.00137

Szirmai, I., Buzsáki, G., & Kamondi, A. (2012). 120 years of hippocampal schaffer collaterals. *Hippocampus*, *22*(7), 1508–1516. https://doi.org/10.1002/hipo.22001

Takács, V. T., Klausberger, T., Somogyi, P., Freund, T. F., & Gulyás, A. I. (2012). Extrinsic and local glutamatergic inputs of the rat hippocampal CA1 area differentially innervate pyramidal cells and interneurons. *Hippocampus*, *22*(6), 1379–1391. https://doi.org/10.1002/hipo.20974

Tao, S., Wang, Y., Peng, J., Zhao, Y., He, X., Yu, X., Liu, Q., Jin, S., & Xu, F. (2021). Whole-Brain mapping the direct inputs of dorsal and ventral CA1 projection neurons. *Front. Neural Circuits*, *15*, 643230. https://doi.org/10.3389/fncir.2021.643230

Teles-Grilo Ruivo, L. M., & Mellor, J. R. (2013). Cholinergic modulation of hippocampal network function. *Front. Synaptic Neurosci.*, *5*, 2. https://doi.org/10.3389/fnsyn.2013.00002

Thomson, A. M., Bannister, A. P., Hughes, D. I., & Pawelzik, H. (2000). Differential sensitivity to zolpidem of IPSPs activated by morphologically identified CA1 interneurons in slices of rat hippocampus: Zolpidem enhancement of basket cell IPSPs in CA1. *European Journal of Neuroscience*, *12*(2), 425–436. https://doi.org/10.1046/j.1460-9568.2000.00915.x

Traub, R. D., Bibbig, A., Fisahn, A., LeBeau, F. E., Whittington, M. A., & Buhl, E. H. (2000). A model of gamma-frequency network oscillations induced in the rat CA3 region by carbachol in vitro. *Eur. J. Neurosci.*, *12*(11), 4093–4106. https://doi.org/10.1046/j.1460-9568.2000.00300.x

Traub, R. D., Miles, R., & Buzsáki, G. (1992). Computer simulation of carbachol-driven rhythmic population oscillations in the CA3 region of the in vitro rat hippocampus. *J. Physiol.* https://doi.org/10.1113/jphysiol.1992.sp019184

Traub, R. D., Miles, R., & Wong, R. S. (1988). Large scale simulations of the hippocampus. *IEEE Eng. Med. Biol. Mag.*, *7*(4), 31–38. https://doi.org/10.1109/51.20378

Traub, R. D., & Miles, R. (1991). *Neuronal networks of the hippocampus*. Cambridge University Press. https://doi.org/10.1017/cbo9780511895401

Tsodyks, M., & Markram, H. (1997). The neural code between neocortical pyramidal neurons depends on neurotransmitter release probability. *Proceedings of the National Academy of Sciences*, *94*(2), 719–723. https://doi.org/10.1073/pnas.94.2.719

Van Geit, W., Gevaert, M., Chindemi, G., Rössert, C., Courcol, J.-D., Muller, E. B., Schürmann, F., Segev, I., & Markram, H. (2016). BluePyOpt: Leveraging open source software and cloud infrastructure to optimise model parameters in neuroscience. *Front. Neuroinform.*, *10*, 17. https://doi.org/10.3389/fninf.2016.00017

Vandecasteele, M., Varga, V., Berényi, A., Papp, E., Barthó, P., Venance, L., Freund, T. F., & Buzsáki, G. (2014). Optogenetic activation of septal cholinergic neurons suppresses sharp wave ripples and enhances theta oscillations in the hippocampus. *Proceedings of the National Academy of Sciences*, *111*(37), 13535–13540. https://doi.org/10.1073/pnas.1411233111

Vanderwolf, C. H. (1969). Hippocampal electrical activity and voluntary movement in the rat. *Electroencephalogr. Clin. Neurophysiol.*, *26*(4), 407–418. https://doi.org/10.1016/0013-4694(69)90092-3

Vida, I., Halasy, K., Szinyei, C., Somogyi, P., & Buhl, E. H. (1998). Unitary IPSPs evoked by interneurons at the stratum radiatum-stratum lacunosum-moleculare border in the CA1 area of the rat hippocampus *in vitro*. *The Journal of Physiology*, *506*(3), 755–773. https://doi.org/10.1111/j.1469-7793.1998.755bv.x

Wang, Q., Ding, S.-L., Li, Y., Royall, J., Feng, D., Lesnar, P., Graddis, N., Naeemi, M., Facer, B., Ho, A., Dolbeare, T., Blanchard, B., Dee, N., Wakeman, W., Hirokawa, K. E., Szafer, A., Sunkin, S. M., Oh, S. W., Bernard, A., . . . Ng, L. (2020). The allen mouse brain common coordinate framework: A 3D reference atlas. *Cell*, *181*(4), 936–953.e20. https://doi.org/10.1016/j.cell.2020.04.007

Wheeler, D. W., White, C. M., Rees, C. L., Komendantov, A. O., Hamilton, D. J., & Ascoli, G. A. (2015). Hippocampome.org: A knowledge base of neuron types in the rodent hippocampus (F. K. Skinner, Ed.) [Publisher: eLife Sciences Publications, Ltd]. *eLife*, *4*, e09960. https://doi.org/10.7554/eLife.09960

Wierenga, C. J., & Wadman, W. J. (2003). Excitatory inputs to CA1 interneurons show selective synaptic dynamics. *Journal of Neurophysiology*, *90*(2), 811–821. https://doi.org/10.1152/jn.00865.2002

Wilkie, D. (1983). Rayleigh test for randomness of circular data. *J. R. Stat. Soc. Ser. C Appl. Stat.*, *32*(3), 311. https://doi.org/10.2307/2347954

1481 Williams, J. H., & Kauer, J. A. (1997). Properties of carbachol-induced oscillatory activity in rat hip-
1482   pocampus. *Journal of Neurophysiology*, *78*(5), 2631–2640. https://doi.org/10.1152/jn.1997.
1483   78.5.2631

1484 Williams, S., & Johnston, D. (1990). Muscarinic depression of synaptic transmission at the hippocampal
1485   mossy fiber synapse. *Journal of Neurophysiology*, *64*(4), 1089–1097. https://doi.org/10.1152/
1486   jn.1990.64.4.1089

1487 Wittner, L., Henze, D. A., Záborszky, L., & Buzsáki, G. (2007). Three-dimensional reconstruction of
1488   the axon arbor of a CA3 pyramidal cell recorded and filled in vivo. *Brain Structure and Function*,
1489   *212*(1), 75–83. https://doi.org/10.1007/s00429-007-0148-y

1490 Yang, D., Ding, C., Qi, G., & Feldmeyer, D. (2021). Cholinergic and adenosinergic modulation of synaptic
1491   release. *Neuroscience*, *456*, 114–130. https://doi.org/10.1016/j.neuroscience.2020.06.006

1492 Yang, S., Yang, S., Moreira, T., Hoffman, G., Carlson, G. C., Bender, K. J., Alger, B. E., & Tang, C.-M.
1493   (2014). Interlamellar CA1 network in the hippocampus. *Proceedings of the National Academy
1494   of Sciences of the United States of America*, *111*(35), 12919–12924. https://doi.org/10.1073/
1495   pnas.1405468111

1496 Ylinen, A., Soltész, I., Bragin, A., Penttonen, M., Sik, A., & Buzsáki, G. (1995). Intracellular corre-
1497   lates of hippocampal theta rhythm in identified pyramidal cells, granule cells, and basket cells.
1498   *Hippocampus*, *5*(1), 78–90. https://doi.org/10.1002/hipo.450050110

1499 Yu, G. J., Bouteiller, J.-M. C., & Berger, T. W. (2020). Topographic organization of correlation along
1500   the longitudinal and transverse axes in rat hippocampal CA3 due to excitatory afferents. *Front.
1501   Comput. Neurosci.*, *14*, 588881. https://doi.org/10.3389/fncom.2020.588881

1502 Yushkevich, P. A., Piven, J., Cody Hazlett, H., Gimpel Smith, R., Ho, S., Gee, J. C., & Gerig, G. (2006).
1503   User-guided 3D active contour segmentation of anatomical structures: Significantly improved
1504   efficiency and reliability. *Neuroimage*, *31*(3), 1116–1128.

1505 Zemankovics, R., Veres, J. M., Oren, I., & Hajos, N. (2013). Feedforward inhibition underlies the prop-
1506   agation of cholinergically induced gamma oscillations from hippocampal CA3 to CA1. *Journal
1507   of Neuroscience*, *33*(30), 12337–12351. https://doi.org/10.1523/JNEUROSCI.3680-12.2013

1508 Zhang, H., Lin, S.-C., & Nicolelis, M. A. L. (2010). Spatiotemporal coupling between hippocampal
1509   acetylcholine release and theta oscillations in vivo. *The Journal of Neuroscience*, *30*(40), 13431–
1510   13440. https://doi.org/10.1523/jneurosci.1144-10.2010

1511 Zisis, E., Keller, D., Kanari, L., Arnaudon, A., Gevaert, M., Delemontex, T., Coste, B., Foni, A., Ab-
1512   dellah, M., Calı, C., Hess, K., Magistretti, P. J., Schürmann, F., & Markram, H. (2021). Dig-
1513   ital reconstruction of the Neuro-Glia-Vascular architecture. *Cereb. Cortex*, *31*(12), 5686–5703.
1514   https://doi.org/10.1093/cercor/bhab254